IJAPLett

IRAQI JOURNAL OF APPLIED PHYSICS LETTERS

IJAPLett

Iraqi Journal of Applied Physics Letters (IJAPLett) is a scientific periodical sponsored and published by the Iraqi Society for Alternative and Renewable Energy Sources and Techniques (I.S.A.R.E.S.T.). The Editorial Board is responsible for the scientific content and other editorial matters relating to the Journal. Manuscripts submitted are first screened by the editors; those on subject matters within the scope of the IJAPLett are sent to an expert referee for evaluation and may be sent to a second reviewer if necessary. This screening process helps to assure an appropriate focus as well as high scientific quality of the Journal. The IJAPLett welcomes submission of papers and letters in applied physics and related fields of science, engineering and technology. They should have something in common with what we now publish on inanimate materials and processes therein: structures, transport, physical, electrical, dielectric, magnetic, and optical properties. Our basic criterion stated below will continue to apply: papers must contain science, especially physics, and there must be an application. We advise authors submitting papers to suggest the names of at least two possible reviewers, with full information on addresses, phone and e-mail. Suggestions of reviewers are welcome regardless of the subject.

AIMS AND SCOPES

Alternative & Renewable Energy
Applied Mechanics & Thermodynamics
Applied Optics & Optical Design
Biophysics & Bioengineering
Cryptography & Applications
Electromagnetic Fields
Electronic Materials & Devices
Energy Generation & Conversion
Fluids Physics & Mechanics
Imaging, Microscopy & Spectroscopy
Laser Physics & Applications
Magnetism & Applications
Instrumentation, Measurements & Metrology
Nanostructures & Applications
Nonlinear & Ultrafast Optics
Nuclear Physics & Engineering
Optical Communications & Systems
Optoelectronics Devices & Applications
Organic Materials, Devices & Applications
Physical Chemistry & Biochemistry
Plasma, Discharge Physics & Applications
Quantum Physics & Spectroscopy
RF & Digital Communications
Semiconductors & Devices
Simulation & Modeling Research
Solar Energy & Devices
Solid State Physics & Applications
Structure & Properties of Matter
Superconductivity & Related Devices
Surfaces, Interfaces & Films
Thin Films & Applications
Vacuum Science & Technology

SPONSORED AND PUBLISHED BY

THE IRAQI SOCIETY FOR ALTERNATIVE AND RENEWABLE ENERGY SOURCES AND TECHNIQUES (I.S.A.R.E.S.T.)

PRINTED IN IRAQ

ISSN 1999-656X

EDITORIAL BOARD

ADVISORY BOARD

This journal is advised by professors and experts at well-known universities and research centers inside Iraq and others abroad:

* * *

  PRINTED IN IRAQ

The Fundamentals of Plasma-Assisted CVD Technique Employed in Thin Films Production

Oday A. Hamadi

P. O. Box 55159,
Baghdad 12001,
Baghdad, IRAQ

This paper reviews the physical and chemical principles of plasma-assisted chemical vapor deposition (CVD) technique for thin films. We focus on the integration, process, and reliability requirements for dielectric films used for isolation, passivation, barrier, and antireflective-coating applications in ultra-large-scale integrated (ULSI) semiconductor circuits.

Keywords: PECVD, Dielectric films, ULSI circuits, Microelectronics production
Received: 20 April 2008, Revised: 20 May 2008, Accepted: 20 June 2008

1. Introduction

The fact that a gas discharge containing charged (ion) and neutral (radical) species can be used to initiate chemical processes has been known for over a century [1]. In later studies, other material-transport phenomena using a high-frequency discharge with an applied external electrode had also been observed [1]. With regard to the latter, the first experimental result, by Anderson in 1962, showed that a radio frequency (rf) voltage can be applied inside a glass tube to create reactive species for thin-film deposition [2]. The following year, Atl et al. showed that this plasma-assisted CVD (or simply "plasma CVD") process could be used for microelectronic applications, especially for diffusion masks and passivation [3,4]. However, the use of plasma-assisted deposition processes for microelectronic circuit manufacturing was not seriously considered until the introduction of commercial batch processing equipment in 1974 [5,6]. Since then, plasma-assisted deposition processing has moved from research and development lines into current product manufacturing lines for integrated circuits (ICs). More research, development, and manufacturing applications of thin films formed by plasma deposition have appeared in the technical literature and various commercial products, especially for microelectronic devices, as discussed in many recent publications [7-11].

In recent years, new materials requirements and lower-processing-temperature requirements in ULSI circuits, solar energy cells, flat-panel displays, and optical systems have made plasma-assisted deposition processes increasingly important. In general, films of silicon-based semiconductors and insulators such as boron-doped or phosphorus-doped and intrinsic amorphous silicon, silicon oxide, phosphorus-doped and/or boron-doped silicon oxide, silicon nitride, and silicon oxynitride deposited by plasma-assisted CVD are most frequently used in solar energy cells [12], xerography [13], thin-film transistors for active-matrix liquid crystal displays [14], and ICs. There are many reviews of plasma deposition processes [15], relevant theory and reaction mechanisms [16], critical issues and parameters [17], and applications in IC fabrication [18].

Five principal types of silicon-based thermal and plasma CVD dielectrics are currently used in IC fabrication: silicon oxide, silicon nitride, silicon oxynitride, phosphorus-doped silicon oxide (PSG), and boron/ phosphorus-doped silicon oxide (BPSG). Their properties can be modified to achieve desirable functions. For example, silicon-rich silicon oxide or nitride films can be used as charge-storage materials for erasable programmable read-only memory (EPROM) devices. The composition of silicon oxynitride can be tailored to meet specific photolithography and etching (or simply "etch") requirements as an antireflective coating (ARC) [19] and also to meet device and integration requirements as a barrier film for gate conductors (to be described later). The gap-filling (or simply "gap-fill") capability and degree of local planarization for high-density plasma (HDP) CVD oxide [20] can be adjusted by changing the deposition-to-sputter-etching ratio (or simply "sputter-etch ratio") D/S, defined as (net deposition rate + blanket sputtering rate)/(blanket sputtering rate). The requirements change for HDP CVD oxide when considering it for use in shallow-trench isolation (STI) compared to use as an intermetal dielectric (IMD). For example, maintaining a wafer temperature less than 400°C is critical for the IMD application for better metal reliability [21].

A higher temperature is desirable for the STI application, since a more dense film that is highly resistant to subsequent wet-etching steps is thus obtained. These applications are discussed in more detail later in the paper.

When tetraethylorthosilicate (TEOS) is used as the silicon source for PECVD oxide deposition, there is less cusping because of the higher surface mobility of the reactants [22]; however, a void still forms if the gap is small enough, because the conformality of the film is not 100%. This means that the amount of deposition on the sidewalls and bottom of the trench portion of a feature is less than on the top of the feature. So, in order to use PECVD films alone for gap-fill applications, they are typically used in conjunction with an argon sputter etch in a multistep PECVD-argon sputter etch-PECVD sequence described previously [23]. Conformal deposition is more typical for thermal (non-plasma) CVD processes such as low-pressure (LP) CVD at high temperatures or for ozone-TEOS atmospheric or subatmospheric pressure (AP or SA) CVD at lower temperatures (less than 600°C). Furthermore, HDP CVD results in a completely different type of profile because of the "bottom-up" deposition from the simultaneous deposition and etching. The resultant topography from any of these CVD processes plays a decisive role in the choice of subsequent planarization techniques. TEOS was the silicon source for the PECVD and the SACVD, and silane for HDP CVD. The typical "bread-loaf" profile of the PECVD oxide film can be adjusted by varying process parameters such as temperature, pressure, and silicon source. The profile of the SACVD oxide film is conformal, and the unique profile of the HDP CVD oxide film is a result of simultaneous etching and deposition. Note that SACVD is a non-plasma process.

Typically, thermal CVD processes such as LPCVD BPSG, APCVD (or SACVD) BPSG, or PSG are used to passivate the polysilicon/metal silicide gate conductor for sub-half-micron devices because of their high-aspect-ratio fill capability compared to plasma CVD processes and because there are no plasma damage concerns with thermal CVD processing. Process-induced IC device damage from plasma processing (in particular at the gate-conductor level, because there is no device protection) is a critical issue for the PECVD passivation dielectrics. Briefly, low process pressure during deposition of the PECVD PSG was identified as the main factor causing gate-oxide charge damage. Increasing the pressure for the PECVD PSG process regardless of dopant source (trimethylphosphite or triethylphosphate) resulted in no charge damage on antenna test sites and device structures. A more recent study describes another technique used to optimize a PECVD PSG process for plasma damage designated as corona oxide semiconductor (COS) charge measurement [24]. The technique, combined with the antenna test structure method of measuring plasma damage, provides a fast and cost-effective way to optimize plasma CVD processes.

Doped silicon oxide films such as PSG or BPSG are preferred for gate-conductor passivation because of their mobile ion barrier properties [25], low reflow temperature for local planarization (applies to BPSG only), high etch selectivity to the underlying barrier layer (e.g., nitride [26]), and faster polishing rate compared to undoped silicon oxide. In this paper, we discuss our recent work with HDP CVD PSG including gap-fill and plasma damage results. We have previously published an overview of our own work and that of others in IBM on relevant thermal CVD processes and applications [27].

The gap-fill requirement for dielectrics in the "back-end-of-line" (BEOL) depends on the interconnect fabrication methods used. Multilevel interconnects usually involve two types of planarization methods: the planarization of interlayer dielectrics and the planarization of metal layers. For the former, for example, an Al(Cu)-based layer is patterned into lines and the insulator is deposited between the spaces and above the lines. Therefore, a critical requirement in this case is the filling of the gaps between the lines without void formation. Void-free filling of high-aspect-ratio features is not a simple matter and requires the use of advanced insulator deposition processes such as HDP CVD. For submicron metal interconnect fabrication, the insulator deposition is generally followed by partial planarization using spin-on-glass (SOG) [28], a resist etch-back [29], or a global planarization using, for example, chemical-mechanical polishing (CMP). For the planarization of metal layers, the damascene technique is most commonly used; several papers reporting its use in IBM have been published [30]. Using this technique, a dielectric such as silicon oxide is deposited on a planar surface and the wiring level is patterned into the dielectric using photolithography and RIE. A thin metal liner and a metal such as tungsten (or aluminum or copper) are then deposited on the patterned dielectric and subsequently planarized by CMP, stopping on the dielectric and leaving metal in the patterned features. Therefore, in the damascene technique, the metal rather than the insulator must fill the high-aspect-ratio features.

A critical film parameter for both interconnect fabrication techniques is the

dielectric constant (k) of the IMD material. Use of a material having a lower dielectric constant leads to lower total capacitance, decreasing the interconnection delay and power dissipation [31], and thus enhancing performance. To achieve long-range interconnection performance objectives, low-dielectric-constant IMD will be required [32]. The dielectric constant of PECVD silicon oxide is typically 4.1-4.2. By doping the oxide with fluorine, the dielectric constant can be reduced to 3.0-3.7, depending on the fluorine concentration [33]. Si-F replaces the Si-OH and Si-H bonds in the oxide; since fluorine is more electronegative, the polarization changes, lowering the dielectric constant. SOG dielectrics (siloxanes, silsesquioxanes) and organic polymers formed by spin coating (polyimides, fluorinated polyimides, bisbenzocyclobutenes), poly(arylethers), or vapor-phase deposition (parylene N, parylene F, teflon) provide dielectric constants in the range of 1.9-3.0 [34]. Most polymers with a dielectric constant less than 3 are stable to only about 350°C. However, a recent publication on laser-evaporated siloxane thin films reports a dielectric constant of 2.0 and thermal stability to 400°C, although integration results were not published [35]. Also, it has been reported that parylene exhibits a high thermal stability [36], and its successful integration into a metal RIE BEOL has been demonstrated [37]. However, damascene integration may be more difficult to achieve because of the softness of parylene films. Spun-on films of materials such as nanoporous silica and xerogels exhibit a higher thermal stability and low dielectric constants (1.3-2.5), depending on their porosity [38], but associated process integration is challenging. There has been increased development activity in plasma-assisted CVD of amorphous carbon and fluorinated carbon films because of their low dielectric constants (2.3-2.7) and thermal stability up to 400°C [39]. Relevant work on insulators having low dielectric constants has been described elsewhere [40].

In this paper, the plasma-assisted CVD of low-dielectric-constant insulators of potential interest at the ULSI level, including fluorine-doped silicon oxide and amorphous carbon and fluorocarbon, was discussed. To be suitable for the deposition of such insulators, plasma-assisted CVD should be applicable at relatively low substrate temperatures, should not damage underlying layers or devices that may be present on the substrate during deposition, and should produce insulators which, in addition to having low dielectric constants, satisfy etching, annealing, planarization, and stability requirements.

2. Fundamentals of PECVD

In thermal CVD, gas-phase reactive species are generated by heating of initial reactants. In plasma CVD, the plasma energy supplied by an external rf source takes the place of the heating to generate the species that subsequently react and deposit on substrate surfaces. Significantly, excessive heating and degradation on the substrate can be avoided by using plasma electron kinetic energy instead of thermal energy. Besides the aspect of generating reactive species at much lower processing temperatures compared to conventional CVD processing, the ion bombardment can be used to modify film characteristics. Plasma CVD processes can be classified into many sub-processes, such as plasma evaporation deposition, plasma sputtering deposition, plasma ion plating, and plasma nitriding. This classification depends on the conditions of the plasma generated, configuration of the vacuum system, location of the substrate, and type of power supply [19-21]. Plasma-assisted CVD processes for semiconductor processing are generally carried out at pressures of 1mTorr to 20Torr substrate temperatures in the range of 100 to 500°C, rf power densities <0.5 W-cm^{-2}, electron densities of 1.0 x 10^{8} to 1.0x10^{12}cm^{-3}, electron mean free paths of <0.1 cm, and average electron energies of 1eV to 6eV.

When the plasma initiates, energy from the rf electric field is coupled into the reactant gases via the kinetic energy of a few free electrons. These electrons gain energy rapidly through the electric field and lose energy slowly through elastic collisions. The high-energy electrons are capable of inelastic collisions that cause the reactant gas molecules to dissociate and ionize, producing secondary electrons by various electron-impact reactions. Table (1) lists typical electron-impact reactions of silane molecules in an rf plasma discharge. In a steady-state discharge, the electrons generated by electron-impact reactions equal those electrons that are lost to the electrode, walls, and reactive species by attachment and recombination reactions [1].

The two important aspects of a plasma glow discharge are the nonequilibrium low-temperature gas-phase chemical reactions that generate radical and ion reactive species in the plasma discharge, and the flux and energy of these reactive species as they reach and strike the surface of the film being deposited. The bombardment of the ionic species on the surface of the film, which controls the surface mobility of the precursor, is the predominant factor in determining film composition, density, stress, and step coverage or conformality at the relatively low temperatures used in plasma CVD. Reactant gases similar to those used for

thermal CVD processes are used for plasma CVD to deposit silicon-based dielectrics at lower deposition temperatures.

Table (1) Typical electron-impact reactions of silane molecules in an rf plasma discharge. The asterisk (*) refers to electronic excited state [1]

Reactant	Reaction products	Enthalpy of formation (eV)
$e^- + SiH_4 \rightarrow$	$SiH_2 + H_2 + e^-$	2.2
	$SiH_3 + H + e^-$	4.0
	$Si + 2H_2 + e^-$	4.2
	$SiH + H_2 + H + e^-$	5.7
	$SiH^* + H_2 + H + e^-$	8.9
	$Si^* + 2H_2 + e^-$	9.5
	$SiH_2 + 2H_2 + 2\ e^-$	11.9
	$SiH_3 + H + 2\ e^-$	12.3
	$Si + 2H_2 + 2\ e^-$	13.6
	$SiH + H_2 + H + e^-$	15.3

2.1 Reaction kinetics

Reactions during plasma deposition are complex and not completely understood. Elementary reactions that occur in plasma have been discussed by various authors [41-43]. The initial reaction between electrons and reactant gas molecules or between reactant gas molecules in plasma can be classified as elastic or inelastic. In the elastic collisions, only minimal translational energy transfer occurs between the gas molecules and reactant gases. For plasma processing, the elastic collisions play a less important role in reactant dissociation. Significantly more translational, rotational, vibrational, and electronically excitational energy transfer occurs in the inelastic collisions. The major inelastic reactions among electrons, reactant gases, and surface that occur during plasma-assisted CVD processing are typically represented in Tables (2-4).

Table (2) Initial electron-impact reactions [1]

Excitation (rotational, vibrational, and electronic)	$e^- + A_2 \rightarrow A_2 + e^-$
Dissociative attachment	$e^- + A_2 \rightarrow A^- + A+ + e^-$
Dissociation	$e^- + A_2 \rightarrow 2A \bullet + e^-$
Ionization	$e^- + A_2 \rightarrow A_2+ + 2e^-$
Dissociative ionization	$e^- + A_2 \rightarrow A+ + A + 2e^-$

Some of the inelastic collisions between inert gases and reactants (such as helium or argon with silane) significantly affect the chemical nature of the discharge and the properties of the deposited films [44-46]. In many plasma deposition processes, inert carrier and diluent gases such as helium and argon have been used to form "cooler" plasma, to create more controlled reaction pathways via Penning reactions between carrier and reactant gases [47], and to suppress gas-phase reactions between reactive species. As a result, a plasma diluted with inert gases such as helium can be used to deposit higher-quality insulators.

Table (3) Inelastic reactions among reactants, inert gases, and substrate. M refers to the inert gas or substrate, and A, B, and C refer to the reactant gases [1]

A	
Penning dissociation	$M^* + A_2 \rightarrow 2A \bullet + M$
Penning ionization	$M^* + A_2 \rightarrow A_2^+ + M + e^-$
Ion-ion recombination	$M^- + A_2^+ \rightarrow A_2 + M$
	or
	$M^- + A_2^+ \rightarrow 2A \bullet + M$
Electron-ion recombination	$e^- + A_2^+ \rightarrow 2A \bullet$
	$e^- + A_2^+ + M \rightarrow A_2 + M$
Charge transfer	$M^+ + A_2 \rightarrow A_2^+ + M$
	$M^- + A_2 \rightarrow A_2^- + M$
B	
Collisional detachment	$M^* + A_2^- \rightarrow A_2 + M + e^-$
Associative detachment	$A^- + A \rightarrow A_2 + e^-$
Atom recombination	$2A + M \rightarrow A_2 + M$
Atom abstraction	$A + BC \rightarrow AB + C$
Atom addition	$A + BC + M \rightarrow ABC + M$

Table (4) Heterogeneous reactions between plasma and surface. S refers to the surface in contact with the plasma, and A and B refer to the reactant gases [1]

Atom recombination	$S - A + A \rightarrow S + A_2$
Metastable de-excitation	$S + M^* \rightarrow S + M$
Atom abstraction	$S - B + A \rightarrow S + AB$
Sputtering	$S - B + M^+ \rightarrow S^+ + B + M$
Surface contact ionization	$S + B^* \rightarrow B^+ + e^- + S$

2.2 Deposition Mechanisms

One of the major advantages of plasma deposition processing is its flexibility for depositing films with desirable properties. For conventional thermal CVD processing, physical and chemical properties of the deposited film pertaining to its stress, conformality, density, moisture resistance, and gap-fill properties can be altered by changing the composition and/or type of reactive species. In plasma-assisted CVD, this can be accomplished by varying deposition parameters such as temperature, rf power, pressure, reactant gas mixture ratio, and type of reactant. For example, silicon oxide films deposited with TEOS generally show higher step coverage or conformality than those deposited

with silane in a plasma-assisted CVD process. For plasma-assisted CVD of silicon oxide films, properties can be modified not only by changing the type of reactive species, but also by the extent of ion bombardment.

In general, the deposition mechanisms for a plasma CVD process can be qualitatively divided into four major steps, as shown in Fig. (1). Step 1 includes the primary initial electron-impact reactions between electron and reactant gases to form ions and radical reactive species (Tables 1 and 2). Next, in step 2, transport of these reactive species occurs from the plasma to the substrate surface concurrently with the occurrence of many elastic and inelastic collisions in both the plasma and sheath regions, classified as ion and radical generation steps [48]. Step 3 is the absorption and/or reaction of reactive species (radical absorption and ion incorporation) onto the substrate surface. Finally, in step 4, the reactive species and/or reaction products incorporate into the deposited films or re-emit from surface back to the gas phase. Because of their complexity, the latter two steps are the least known and least studied aspects of plasma CVD. Significant roles are played by ion bombardment [49] and various heterogeneous reactions between ions and radicals with the depositing surface in the sheath region. The two steps critically affect film properties such as conformality [50], density, stress [51], and "impurity" incorporation.

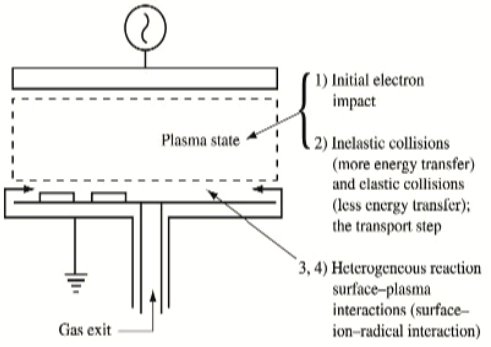

Fig. (1) Four steps that characterize the mechanisms of plasma CVD process [1]

Plasma CVD of amorphous and microcrystalline silicon are the most studied plasma CVD processes, with hundreds of publications on their deposition kinetics and mechanisms. The basic gas-phase chemistry of the silane plasma has been studied by various techniques [49-52]. Different mechanisms have been suggested for the dominant reaction pathway of silicon deposition. One mechanism describes SiH_3 (silyl) radicals playing a dominant role [53], while others describe the decomposition of silane to SiH_2 (silylene) and then SiH_2 insertion into gas-phase SiH_4 to form higher silane species [54] as the main silicon deposition mechanism.

4. Conclusions

We have reviewed the plasma-assisted CVD of dielectric films, with an emphasis on aspects relevant to ULSI semiconductor circuits. In addition, we have indicated that manufacturing needs must be considered early in the process and tool development phase. Obviously, the ultimate goal is to optimize a plasma CVD process for a particular application at the lowest cost of ownership. Future research and development must focus not only on specific technical issues that arise with each new IC generation (such as integration of a stable low-*k* IMD into the BEOL), but also on manufacturability and cost. With 300mm-diameter wafers containing sub-0.25µm semiconductor IC circuits on the horizon, the technical and manufacturing issues are daunting; new challenges are presented to both the semiconductor manufacturers and their equipment suppliers, even for the conventional processes used in IC production.

References

1. S.V. Nguyen, **"Plasma-Assisted Chemical Vapor Deposition",** *Handbook of Thin-Film Deposition Processes and Techniques,* K.K. Schuegraf, Ed., Noyes Publications, Park Ridge, NJ, 1988, pp. 112-141.
2. G.S. Anderson, *J. Appl. Phys.* 33, No. 10, 2991-2992 (1962).
3. L.L. Atl, S.W. Ing, Jr. and K.W. Laendle, *J. Electrochem. Soc.* 110, 465 (1963).
4. S.W. Ing, Jr. and W. Davern, *J. Electrochem. Soc.* 111, 120-122 (1964).
5. A.R. Reinbergh, *Ann. Rev. Mater. Sci.* 9, 341-372 (1979).
6. D.E. Carlson, C.W. Magee and A.R. Triano, *J. Electrochem. Soc.: Solid-State Sci. Technol.* 126, No. 4, 688-691 (1979).
7. S. Sherman et al., *J. Electrochem. Soc.* 144, No. 9, 3198-3204 (1997).
8. H. Randhawa, *Thin Solid Films* 196, 329-349 (1991).
9. J.A. Thornton, *Thin Solid Films* 107, 3-19 (1983).
10. A.T. Bell, *J. Vac. Sci. Technol.* 16, No. 2, 418-419 (1979).
11. R.F. Bunshah, *IEEE Trans. Plasma Sci.* 18, 846-854 (1990).
12. A. Sherman, *Thin Solid Films* 113, 135-149 (1984).
13. S.V. Nguyen, *J. Vac. Sci. Technol. B* 4, No. 5, 1159-1167 (1986).
14. C. Bencher et al., *Solid State Technol.* 40, No. 3, 109-114 (1997).

15. B.L. Chin and E.P. van de Ven, *Solid State Technol.* 31, 119-122 (1988).
16. A.K. Stamper, J.B. Lasky and J.W. Adkisson, *J. Vac. Sci. Technol. A* 13, 905-911 (1995).
17. E. Yon, W.H. Ko and A.B. Kuper, *IEEE Trans. Electron Devices* ED-13, 276-280 (1966).
18. N. Ikegami, N. Ozawa, Y. Miyakawa and J. Kanamori, *Jpn. J. Appl. Phys.* 30, 1556-1561 (1991).
19. A. Adams and C. Capio, *J. Electrochem. Soc.* 128, 423-429 (1981).
20. S. P. Murarka, *Solid State Technol.* 39, No. 3, 83-90 (1996).
21. T. Fujii et al., *J. Vac. Sci. Technol. B* 15, No. 3, 746-749 (1997).
22. K. Endo and T. Tatsumi, *Appl. Phys. Lett.* 70, No. 19, 2616-2618 (1997).
23. P.S. Andry, P.W. Pastel and W.J. Varhue, *J. Mater. Res.* 11, No. 1, 221-228 (1996).
24. L.H. Chou and W.T. Hsieh, *J. Appl. Phys.* 75, No. 4, 2257-2263 (1994).
25. S.P. Murarka, *Mater. Sci. Eng.* R19, No. 3-4, 87-151 (1997).
26. G. Lucovsky, *Adv. Mater. Opt. Electron.* 6, 55-72 (1996).
27. J. Batey and E. Tierney, *J. Appl. Phys.* 60, No. 9, 3136-3145 (1986).
28. G. Turban, *Pure & Appl. Chem.* 56, No. 2, 215-230 (1984).
29. H.F. Winter, *Topics in Current Chemistry: Plasma Chemistry III,* S. Verpek and M. Venugopulan, Eds., Springer-Verlag, Berlin, 1980, pp. 65-112.
30. G. Carter and G.S. Calligan, **"Ion Bombardment of Solids**", American Elsevier, New York, 1969.
31. J.R. Hollahan and A.T. Bell, "**Techniques and Applications of Plasma Chemistry"**, John Wiley & Sons, New York, 1974.
32. S.V. Nguyen et al., *Thin Solid Films* 193/194, 595-609 (1990).
33. A.A. Bright, *J. Vac. Sci. Technol. A* 9, No. 3, 1088-1093 (1991).
34. D. Tsu, G. Parsons and G. Lucovsky, *J. Vac. Sci. Technol. A* 6, No. 3, 1849-1854 (1988).
35. J.D. Chapple-Sokol et al., *J. Electrochem. Soc.* 138, No. 12, 3723-3726 (1991).
36. R. Winkler et al., *Plasma Chem. Plasma Process.* 10, No. 3, 419-442 (1990).
37. H. Dun et al., *J. Electrochem. Soc.* 128, No. 7, 1555-1563 (1981).
38. W.A.P. Claassen, *Plasma Chem. Plasma Process.* 7, No. 1, 109-124 (1987).
39. A. Yuuki, Y. Matsui and K. Tachibani, *Jpn. J. Appl. Phys.* 28, No. 2, 212-218 (1989).
40. S. Miyazaki et al., *Jpn. J. Appl. Phys.* 30, No. 7, 1539-1544 (1991).
41. C.-P. Chang, C.S. Pai and J.J. Hsieh, *J. Appl. Phys.* 67, No. 4, 2119-2126 (1990).
42. E.R. Mosburg, Jr., R.C. Kerns and J.R. Abelson, *J. Appl. Phys.* 54, No. 9, 4916-4927 (1983).
43. F.J. Kampas, "Chemical Reactions in Plasma Deposition," *Semiconductors and Semimetals,* Vol. 21A, J. I. Pankove, Ed., Academic Press, Inc. (NY), 1984, Ch. 8.
44. D. Mataras, S. Cavadias and D. Rapakoulias, *J. Appl. Phys.* 66, No. 1, 119-124 (1989).
45. N. Itabashi et al., *Jpn. J. Appl. Phys.* 29, No. 3, L.505-L.507 (1990).
46. H.A. Weakliem, "Diagnostics of Silane Glow Discharges Using Probes and Mass Spectroscopy," *Semiconductors and Semimetals,* Vol. 21A, J. I. Pankove, Ed., Academic Press, Inc. (NY), 1984, Ch. 10.
47. N. Hata, A. Matsuda and K. Tanaka, *J. Non-Cryst. Solids* 59-60, 667-670 (1983).
48. S.M. Han and E.S. Aydil, *Thin Solid Films* 290-291, 427-434 (1996).
49. R. Robertson and A. Gallager, *J. Appl. Phys.* 59, No. 10, 3402-3411 (1986).
50. A. Matsuda and K. Tanaka, *J. Appl. Phys.* 60, No. 7, 2351-2356 (1986).
51. P.A. Longeway, R.D. Estes and H.A. Weakliem, *J. Phys. Chem.* 88, 73-77 (1984).
52. M. Heintze and S. Veprek, *Appl. Phys. Lett.* 54, No. 14, 1320-1322 (1989).
53. S. Meikle, Y. Nakanishi and Y. Hatanaka, *Jpn. J. Appl. Phys.* 29, No. 11, L2130-L2132 (1990).
54. A. Gallager, *J. Appl. Phys.* 63, No. 7, 2406-2413 (1988).

Khalid F. Al-Zubaidi
Aseel M. Al-Taiee
Raheem A. Hameed

Department of Mechanical Engineering, College of Engineering, University of Kufa, Kufa, IRAQ

Using Longitudinal Surface Acoustic Waves for Non-Destructive Testing of Inner Surfaces

In this paper, experimental results of nondestructive ultrasonic testing using longitudinal surface waves (LSAW) were presented. Analysis of real LSAW signals, generated and received by angle transducers, was performed and causes of lateral interference were investigated, optimal angle transducer constructions were offered. Real angle transducer parameters and levels of LSAW signals, reflected from artificial defects in duralumin sample, were evaluated. It was concluded by experimental investigations that LSAW signal magnitude and collateral interference level ratio reaches 24dB. This gives opportunity to perform sufficiently reliable shell product inner surface nondestructive testing using secondary longitudinal surface waves.

Keywords: Non-destructive test, LSAW, Ultrasonic waves, Acoustics
Received: 20 April 2008, Revised: 20 May 2008, Accepted: 20 June 2008

1. Introduction

Excitation of secondary longitudinal surface acoustic waves (LSAW II) on the opposite side of the plate during propagation of primary LSAW (LSAW I) [2, 3] on the first surface is one of the exceptional features of LSAW [1-3]. That permits analysis and detection of surface defects located on inaccessible inner surface of the sheet products, such as tanks, reservoirs, boilers and also nuclear reactor components [4, 5], using secondary LSAW. There are some reservations about application possibilities of the secondary LSAW in non-destructive tests under real conditions, considering natural attenuation of LSAW, highly exceeding attenuation of Rayleigh waves. The purpose of this work was to investigate experimentally the parameters of the real secondary LSAW signals and to determine the potential limits for shell product inner surface analysis.

2. Methodology and Equipment

It was experimentally determined that LSAW are excited most effectively using variable angle prismatic transducers [6,7]. The earlier described digital ultrasonic defectoscope was used in experiments; it incorporates 2-4 MHz variable angle prismatic piezoelectric transducers [7]. The secondary LSAW (LSAW II) excitation and investigation scheme for this case is shown in Fig. (1).

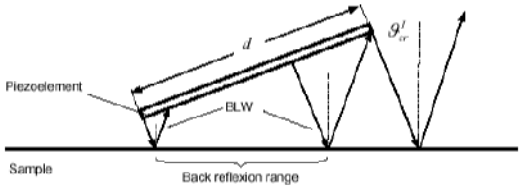

Fig. (1) LSAW II experimental investigation scheme

The angle emitter matched for the first critical angle ϑ^{I}_{cr} is excited using the pulse generator and it generates LSAW I in the test sample. Bulk transversal waves (BTW) propagate and at the same time generate LSAW II on the opposite side. During investigation these waves can be picked up by the angle receiver placed on the inner surface of the product. Notches of 1 mm width and of the different depth (from 2 to 4 mm) are made on the inner surface in order to simulate the defects. The receiver placed on the bottom position is turned around by 180 (Fig. 1, dashed line) in order to receive the LSAW II, reflected from the notch. Features of LSAW signal pick-up using angle transducer Reception of the LSAW signals by the variable angle transducer is associated with a series of problems. One of them is the duplication of the acoustic pulse excited by a piezoelement generating the plane bulk longitudinal wave (BLW). Duplication of the acoustic pulse is due to the small LSAW excitation angle [8]

$$\vartheta^I_{cr} = \arcsin\left(\frac{c'_L}{c''_L}\right) \qquad (1)$$

where c'_L and c''_L are velocities of bulk longitudinal wave in the angle transducer prism and the sample respectively. For example, the LSAW is generated in duralumin (c''_L=6320m/s) products using the transducer with the prism, manufactured of plexi glass (c'_L=2730m/s), ϑ^I_{cr}=25.6. In the case when the dimension of the piezoelement generating the plane BLW $d>>\lambda_L$, where λ_L is the length of the longitudinal waves in the prism, conditions may arise for excitation of piezoelement repeatedly by the reflected BLW pulse (Fig. 2).

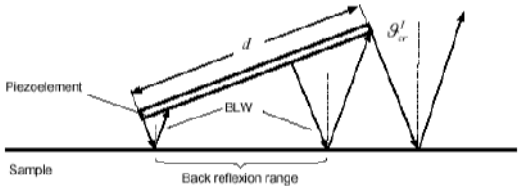

Fig. (2) Scheme of repeated excitation of piezoelement

The LSAW pulses of an identical shape are generated because of repeated excitation of the piezoelement by the BLW pulse, reflected from the surface of the sample (Fig. 3). Besides, the magnitude of the second LSAW pulse may be sometimes even higher than of the first, although it is created by the pulse reflected from the surface of the test sample, consequently weaker than the first BLW pulse. This paradox is explained in the following way. First, when piezoelement is excited by the electric pulse the it emits the acoustic pulse, shape of which is determined by piezoelement pulse response. Thus, shape of the BLW pulse reflected from the surface ideally matches the pulse response of the piezoelement; for this reason efficiency of the repeated excitation (acoustic) is maximal. Second, if the transducer incidence angle ϑ is not exactly equal to ϑ^I_{cr}, then the LSAW II pulse may be emitted at the angle, closer to ϑ^I_{cr}, therefore, it may be stronger than the first one.
The second pulse of the BLW signal may be eliminated increasing piezoelement distance from the radiating prism plane, using standard double transducers with an acoustic delay and an additional prism (Fig. 4). However, in such case transducers sensitivity would decrease and transducers dimensions would increase due to the increased BLW attenuation in the prism. It can be even useful as an indication that received acoustic signal is the LSAW signal, not a lateral reflection of the BLW in an angle transducer prism or in the analyzed sample.

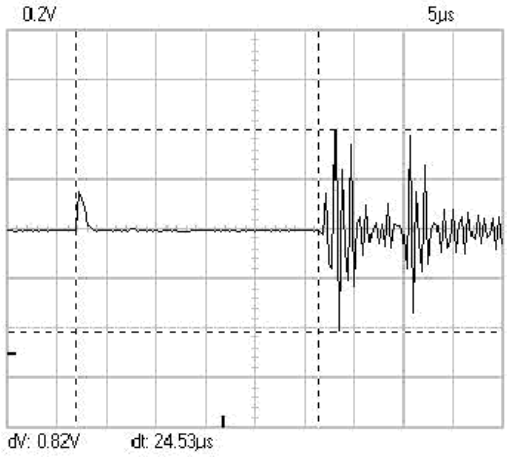

Fig. (3) Duplicated LSAW signal, generated as a result of repeated excitation of the piezoelement. Thickness of the sample D=40mm

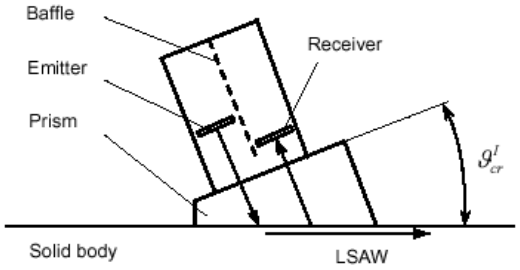

Fig. (4) LSAW angle transducer with additional prism Noticeably, the duplication of acoustic signal does not influence measurements or NDT using LSAW

Another lateral effect, natural to investigations of LSAW, is associated with back radiation (pick-up) of the angle type transducer. It was found experimentally that the angle type transducer radiates (receives) LSAW not only in the forward direction, but also in the reverse direction. The measured ratio of transducer sensitivities in the forward and the reverse directions is 23.5 dB. Collateral forward LSAW pulses can be seen on oscilloscope display due to reception in the reverse direction, when the LSAW signals, reflected from the defect, are received using the experimental set-up, shown in Fig. (1). They are observed in the time domain earlier than the LSAW pulses reflected from the defect, which have traveled a longer distance (Fig. 5).

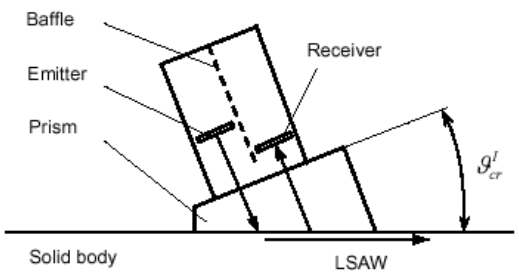

Fig. (5) LSAW signal on the display of a digital oscilloscope: (1) LSAW, pulse, reflected from the defect; (2) duplicated collateral (forward) LSAW pulses, picked by the receiver in the reverse direction; (3) repeated piezoelement excitation pulse, reflected from the defect

Especially negative factor is that collateral pulses are the first on the time axis. Interpretation of a complex signal can be complicated and may lead to non-destructive testing errors, if collateral reverse reception signals are significant in a magnitude. In such cases unwanted reverse reception signals can be eliminated using the angle transducer with two identical piezoelement (Fig. 6) and introducing the reception channel, using electronic gate blocking for a time interval

$$\Delta t \geq 2(\Delta t_{1L} + \Delta t_{1T}) + 2(\Delta t_{2L} + \Delta t_{2T}) + \Delta t^{II}_{PIB} \qquad (2)$$

where Δt_{1L} and $\Delta t_{2L}$are respectively the first piezoelement (emitter) radiated and the second piezoelement (receiver) received BLW pulse delay times in the prism; Δt_{1T} and Δt_{2T} are respectively the first and the second piezo-crystal BTW pulse delay times in the sample; Δt^{II}_{PIB} is the delay time of the LSAW II signals, when they propagate between the points A and B.

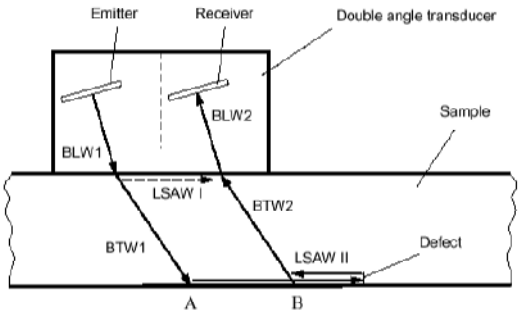

Fig. (6) Double angle transducer In this case the LSAW signal, reflected from the surface defect or sample edge is the first received ultrasonic signal, observed on an oscilloscope display

3. Results and Discussion

Set-up used for experimental investigations is shown in Fig. (1). After determining the value of the first critical angle ϑ^1_{cr}=25,6, two identical fixed angle transducers were made where the piezoelement are acoustically damped. The transducer maximum sensitivity frequency is 2,5 MHz. LSAW-II signal excited by one of these transducers and received by another on is shown in Fig. (7), in which LSAW II signal received by the angle transducer (1) at 2.5MHz, propagating in the forward direction.

When pick-up transducer is turned around by 180, the LSAW II signals reflected from the artificial defect (1mm width, h=2mm depth notch) are registered by it, and the different distances from the defect are selected (Fig. 8). The first two lower magnitude pulses are collateral LSAW II signals, propagating in the direction of the defect and received by the reverse side of the angle transducer. When the transducer is moved closer to the defect, the LSAW II signal reflected from it moves along sweep origin direction, and when L=0 its magnitude is maximal (Fig 8b). When the transducer is behind the defect, there is no LSAW II signal, reflected from the defect; only duplicated collateral pulses are left (Fig. 8d).

When the inner surfaces of sheet type products are investigated using LSAW II, these waves have to be excited and received up from the outer surface side by the same angle transducer or using the double transducer (Fig. 4, Fig. 6). Scheme of such investigation is shown in Fig. (9), and the LSAW II signal reflected from the defect in Fig. (10).

In this case there are no signals received by the reverse side of pick-up element. Although LSAW II signal and the hardware interference ratio (16-24 dB) is less than during investigation using two separate transducers (~40dB), it is still sufficiently large to register the defect reliably. In the sheet sample with the thickness D=10mm, due to multiple signal reflections between the walls and due to small BTW attenuation in duralumin, the received acoustic signal is strong and consists of long series of LSAW II waves, reflected from the defect (Fig. 11). This indicates, that it could be possible to use higher than 2.5MHz frequency angle transducers for sheet products, which would allow to increase the investigation accuracy and to detect smaller defects.

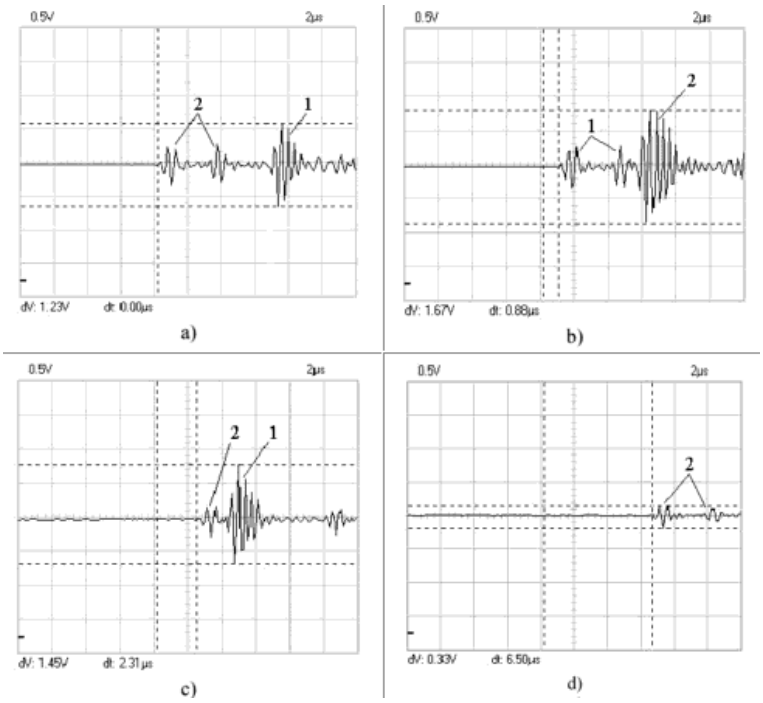

Fig. (8) LSAW II signals (1), reflected from the sample notch (h=2mm); signals (2) received at the reverse direction of transducer. Distance L from pick-up aperture center to defect: (a) +4mm (b) 0 (c) -19mm (d) -48mm

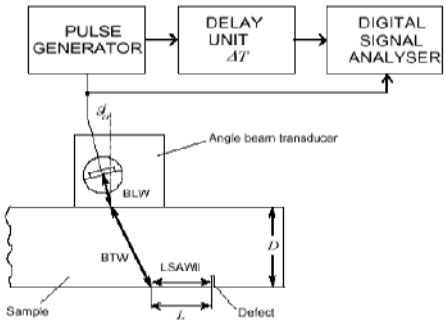

Fig. (9) Scheme of inner surface investigation using LSAW II

It should be noticed, that only a part of LSAW II energy is reflected from 2mm depth notch (defect), and the magnitude of the received LSAW II signal is significantly greater (~3dB) when defect is deeper (h=4mm) (Fig. 11, b). That confirms LSAW property to propagate in a near-surface layer.

Since the angle type transducer radiates directional LSAW, it is naturally that the magnitude of the signal reflected from a regular shape defect (smooth notch) depends on the defect orientation with respect to the LSAW propagation direction. Therefore, detection probability of defects of such nature is higher for the defects, orientation of which can be foreseen (e. g., for defects along welding juncture). The described investigations were performed by the angle transducer, directional characteristic width of which in the plane of sample surface measured at the 3dB level was 3-40.

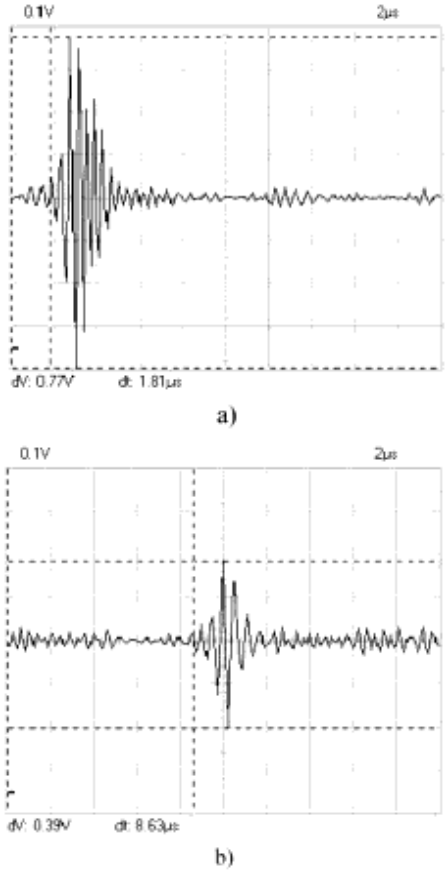

Fig. (10) LSAW II signal, reflected from the inner defect, when D=40mm and the distance L (a) 0 (b) 20mm

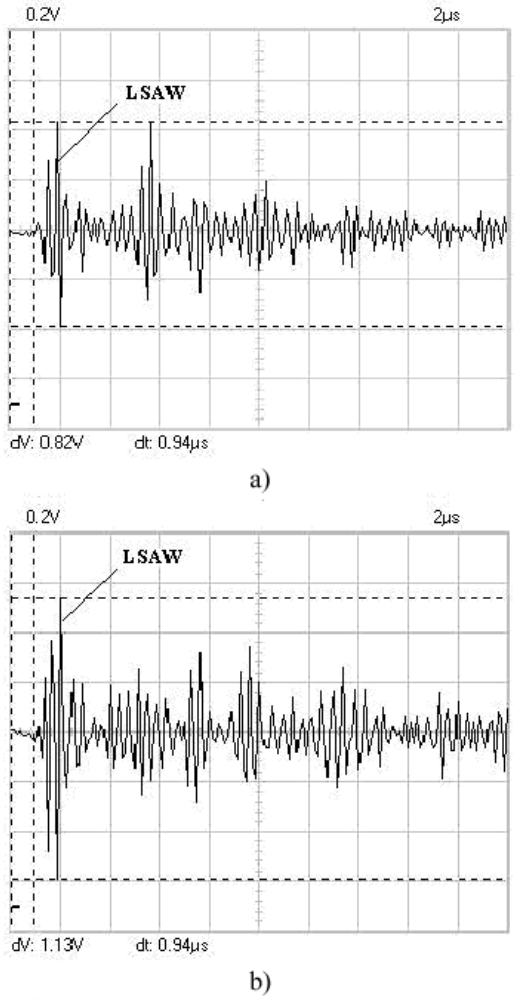

Fig. (11) LSAW II signals, reflected from notch in plate with thickness D=10mm. Depth of notch (defect) h: (a) 2mm (b) 4mm

4. Conclusions

The level of LSAW II signals excited and picked up by angle transducers is less than the level of LSAW I by 10^{15}dB, but it is still sufficient in order to perform non-destructive ultrasonic testing of shells and inner walls of sheet type product (tanks, boilers). Double angle transducers are the most efficient for registration of LSAW II in products with known acoustic properties. LSAW II non-destructive testing is more efficient for investigation of regular shape defects (cracks) with predictable orientation, for example, along welded joint.

References

1. H. Arwin, *Appl. Spectrosc.*, 40 (1986) 313-318.
2. E. Gizeli et al., *IEEE Trans. Ultrason. Ferroelect. Freq. Contr.*, 39 (1992) 657-659.
3. J. Kondoh and S. Shiokawa, *Electr. Comm. Japan*, 76 (1993) 224-234.
4. Z. Wang and J. D.N. Cheeke, *Appl. Phys. Lett.*, 64 (1994) 2940-2942.
5. J. Du et al., *Sensors Actuators*, A56 (1996) 211-219.
6. B. Jakoby and M.J. Vellekoop, *IEEE Trans. Ultrason. Ferroelect. Freq. Contr.*, 45 (1998) 1293-1302.
7. A. Santos and D.E. Bray, *Rev. Sci. Instrum.,* 71(9) (2000) 3464-3469.
8. S. Sajauskas, A. Valinevičius and L. Miežutavičiūtė, *Ultrasound*, 1(54) (2005) 12–16.

Comparative Evaluation of Bit Error Rate in Frequency Selective Fading Channels Employed in Wavelet Modulation

Sahra S. Jassem

School of Applied Sciences, University of Technology, Baghdad, IRAQ

In this work, results of a comparison modeling treatment of additive white Gaussian noise and two-ray fading channel those affecting the performance of modulation techniques employed in modern communications systems, were presented. The channel parameters were varied to obtain a frequency-selective channel, which was observed by determining the bit error rate as a function of the ratio of signal energy per bit to thermal noise power per Hz. This treatment introduces the performance of wavelet modulation employing such systems.

Keywords: Wavelet modulation, Rayleigh fading channel, Frequency selective channel
Received: 20 April 2008, Revised: 20 May 2008, Accepted: 20 June 2008

1. Introduction

A promising application of wavelet transforms is in the field of digital wireless communications where they can be used to generate waveforms that are suitable for transmission over wireless channels. This type of modulation is known as wavelet modulation (WM) or fractal modulation. The advantage of this scheme emerges from the fact that wavelet modulation allows transmission of the data signal at multiple rates simultaneously.

Wornell and Oppenheim outlined the design of the transmitter and receiver for wavelet modulation (WM) [1]. The performance of wavelet modulation in an additive, white Gaussian noise (AWGN) channel was also evaluated in Ref. [1]. Wornell showed that the bit error rate (BER) performance of wavelet modulation is a function of signal-to-noise ratio (SNR) in the channel; the estimate of the received bit becomes more accurate as the number of noisy observations used to calculate it is increased. Ptasinski and Fellman simulated wavelet modulation using the Daubechies N=4 wavelet and measured its BER performance in an AWGN channel [2]. The performance of wavelet modulation was shown to be equivalent to that calculated by Ref. [1] (i.e. the results were equivalent to binary phase shift keying (BPSK) performance for the AWGN channel) [2]. In all of the previous research, the BER performance was measured using a single scale (i.e. rate) for demodulation.

Wavelets have also been proposed for use in other aspects of communication systems. Multiple access schemes using orthogonal wavelet-based codes have been proposed as an alternative to code division multiple access (CDMA) [3,4]. Wavelet-based modulation techniques for frequency-hopped spread spectrum communications have also appeared in the literature [5,6] as the wavelet packet transform. An extension of the wavelet transform, in which the high pass branches are iterated as well as the low pass branches, has led to the development of wavelet packet modulation (WPM). This modulation technique exploits the larger selection of time-frequency tailings at its disposal to minimize channel disturbances [7,8].

A fading channel is modeled with a multiplicative fading component and an additive noise component. The order of simulation complexity for such a process for 1-D modulations is one addition and one multiplication. For 2-D modulation methods, the complexity for one symbol is one complex multiplication and one complex addition per symbol. This is equivalent to four real multiplications and four real additions for each symbol [9].

2. Modeling Procedure

Clarke [5] has proposed a statistical model for the received signal amplitude of the flat-fading channel based on scattering propagation. Gans [10] has further shown that in the case of isotropic, two-dimensional scattering with an omni-directional receiving antenna, the quadrature Gaussian processes representing the fading have autocorrelation function (ACF) [11].

The most common channel model encountered in communications systems is the additive white Gaussian noise (AWGN) channel. In this channel, zero-mean white Gaussian noise is added to the transmitted signal $s(t)$, so that the received signal $r(t)$ can be represented as:

$$r(t) = s(t) + n(t) \quad (1)$$

where $n(t)$ is a zero-mean white Gaussian noise process. $N_o/2$ is the power spectral density of the noise term $n(t)$.

The time dispersion in a multi-path environment causes the signal to undergo either flat or frequency selective fading. If the channel has a constant gain and linear phase response over a bandwidth that is greater than the bandwidth of the transmitted signal, then the received signal undergoes flat fading (i.e. the received signal is not distorted by inter-symbol interference). In a flat fading, channel the signal bandwidth is much smaller than the coherence bandwidth of the channel. Alternatively, time dispersion can be described in terms of the symbol period (T_S). In a flat fading, channel T_S is much larger than the root-mean-square (r.m.s) delay spread of the channel (σ_τ). In these wavelet modulation trials T_S at scale 10 is 0.977ms and T_S at scale 13 is 122µs. The form of this simulated model, Eq. (2), results in a flat fading channel for all scales (i.e. $\sigma_\tau << T_{S13} < T_{S10}$) since σ_τ is effectively zero in this model.

Small scale fading can be modeled as a Rayleigh distribution [12,13]. The received signal is given by

$$r(t) = s(t)R(t) + n(t) \quad (2)$$

As in the AWGN channel, $s(t)$ is the transmitted signal and $n(t)$ represents thermal and device noise (it also still dictates the SNR). The impact of the Rayleigh, flat, slow fading channel is given by the multiplicative $R(t)$ [12]. The function $r(t)$ is coherently demodulated; perfect carrier synchronization is assumed at the receiver.

If the bandwidth of the signal of interest exceeds the coherence bandwidth of the channel, the signal undergoes frequency selective fading. In the frequency domain, the channel causes different levels of attenuation for different frequency components of the signal. Frequency selective fading is caused by multi-path delays which approach or exceed the symbol period of the transmitted symbol (i.e. $T_S < \sigma_\tau$), where σ_τ is still the r.m.s delay spread of the channel. In practice, $T_S \leq 10\sigma_\tau$ will result in a frequency selective channel as the channel introduces ISI.

I have used a two-ray channel model with a variable r.m.s delay spread σ_τ. (σ_τ was varied between 0.2µs and 120µs). In propagation measurements by Reference [14] at 900MHz, urban areas typically had r.m.s delays in the range of 2−3µs, hilly residential areas had r.m.s delays in the range of 5−7µs and worst case r.m.s delay spreads were of the order of 20µs. Excess delays in the range of 100µs were also observed. For the frequency selective fading channel, the received signal is given by:

$$r(t) = \alpha_0 R_0(t)s(t) + \alpha_1 R_1(t)s(t-\tau_1) + n(t) \quad (3)$$

where α_0 and α_1 are the amplitudes of the main ray and the secondary ray, respectively.

The signal energy in the main component along with the power of the noise term, $n(t)$, determines the SNR of the signal. The secondary component with a factor of α_1 and delayed by τ_1 corresponds to the first multi-path bin with significant amplitude.

The r.m.s delay spread is defined as [12]:

$$\sigma_\tau = \sqrt{\overline{\tau^2} - (\overline{\tau})^2} \quad (4)$$

where τ is the mean excess delay and is defined by:

$$\overline{\tau} = \frac{\sum_k P(\tau_k)\tau_k}{\sum_k P(\tau_k)} \quad (5)$$

where $P(\tau_k)$ is the power of the k^{th} component (ray) and is obtained from the power delay profile of the channel and τ_k is the delay of the k^{th} component. All delays are measured relative to the first signal arriving at τ_0=0. The second moment of the power delay profile (τ_2) is given by:

$$\overline{\tau^2} = \frac{\sum_k P(\tau_k)\tau_k^2}{\sum_k P(\tau_k)} \quad (6)$$

For these experiments, I simulate two paths so that k=0 and k=1. Furthermore, in many of these trials, $\alpha_0 = \alpha_1$; thus Eq. (4) simplifies to $\sigma_\tau = \tau_2$. Now, $P(\tau_k)$ is given by α_{2k} where α_k is the amplitude (gain) of the k^{th} ray.

The sum of $E\{\alpha^2_0 R_0(t)^2\}$ and $E\{\alpha^2_1 R_1(t)^2\}$ is set to unity so that the channel has an average power gain of one [15]. This is to ensure that the average signal energy at the input and output of the channel remains the same. A generalized block diagram of a frequency selective channel is shown in Fig. (1) for an N-path channel. For frequency-selective channel in (3), N=2 [12].

In Fig. (1), the Rayleigh waveform $R_{N-1}(t)$ can be generated using Clarke [5] and Gans [10] fading model. A Rayleigh fading waveform can be simulated by generating independent in-phase and quadrature complex Gaussian noise samples and filtering them by $H(f)$ as shown in Fig. (2). $S_{Ez}(f)$ is the spectrum of the Doppler filter. Particularly, it has been shown that for an omni-directional λ/4 antenna with a gain of 1.5, the Doppler spectrum is given by [16]:

$$S_{E_z}(f) = \frac{1.5}{\pi f_m \sqrt{1 - (\frac{f - f_c}{f_m})^2}} \quad (7)$$

where f_c is the center frequency and f_m is the maximum Doppler spread. The frequency f_c is

zero and f_m takes values of 60Hz and 120Hz. The sum of the in-phase and quadrature terms at the output of the inverse fast Fourier transformation (IFFT) forms the complex Rayleigh fading waveform $R_{N-1}(t)$. The waveform has a Rayleigh distributed amplitude and a uniformly distributed phase in the interval [0,2π). The r.m.s value of the envelope is normalized to one. This normalization ensures that the average signal energy is not altered when passed through the channel simulator. This complex, normalized waveform is denoted as $R_{N-1}(t)$ in Fig. (2). These Rayleigh waveform generators are used to generate each of the $R_k(t)$ in Fig. (1) where k is from 0 to N-1. The waveform $R(t)$ in Eq. (2) is obtained by taking only the envelope component (i.e. $R(t)=|R_{N-1}(t)|$) of the complex fading waveform generated in Fig. (2).

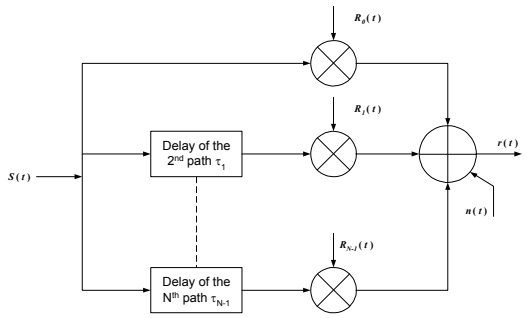

Fig. (1) Frequency-selective channel model

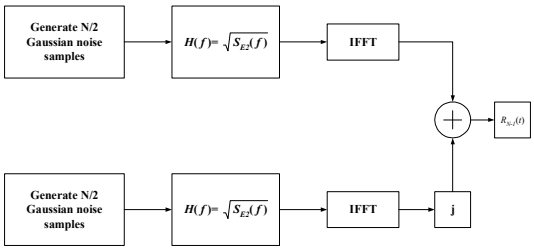

Fig. (2) Generation of a Rayleigh fading waveform

The wavelet representation of a signal $s(t)$ is given by [16]:

$$s_n^m = \int_{-\infty}^{\infty} s(t) 2^{m/2} \psi(2^m t - n) dt \qquad (8a)$$

$$s(t) = \sum_{m=-\infty}^{\infty} \sum_{n=-\infty}^{\infty} s_n^m 2^{m/2} \psi(2^m t - n) \qquad (8b)$$

where $\psi(t)$ is the wavelet function [17].

The resolution limited approximation of a signal $s(t)$ is given by

$$A_{m+1} s(t) = \sum_n a_n^{m+1} \phi_n^{m+1}(t) \qquad (9)$$

where the function a_n^{m+1} produces the approximation coefficients obtained by the projection of $s(t)$ onto the basis functions:

$$a_n^{m+1} = \int_{-\infty}^{\infty} s(t) \phi_n^{m+1}(t) dt \qquad (10)$$

The approximation and wavelet coefficients can be calculated at any scale by:

$$a_n^m = \sum_l h(1-2n) a_l^{m+1} \qquad (11a)$$

$$s_n^m = \sum_l g(1-2n) a_l^{m+1} \qquad (11b)$$

where $h(-n)$ and $g(-n)$ are the low-pass and high-pass filters in the associated 2 channel analysis filter bank. Eq.s (10a) and (10b) represent the fast wavelet transform (FWT) needed to compute the discrete wavelet transform (DWT) in Eq. (8) and Fig. (3) shows the analysis filter bank corresponding to the DWT.

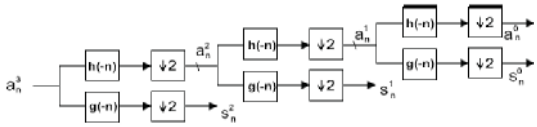

Fig. (3) A two-channel analysis filter bank used to compute the DWT

Conversely, it is possible to reconstruct the approximation coefficients a_n^m using the following equation:

$$a_n^{m+1} = \sum_l h(2l-n) a_l^m + g(2l-n) s_l^m \qquad (12)$$

The reconstruction process is shown in Fig. (4). This is the inverse FWT (IFWT) needed for computing the inverse DWT (IDWT) in Eq. (8b). In Fig. (4), $h(n)$ and $g(n)$ are the low-pass and high-pass synthesis filters. The low-pass filter ($h(n)$) satisfies the following orthogonality condition:

$$\sum_n h(n) h(n-2k) = \delta(k) \qquad (13)$$

The highpass filter is obtained from the low-pass filter by:

$$g(n) = (-1)^n h(N-n) \qquad (14)$$

where $(N+1)$ is the filter length.

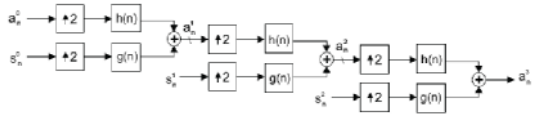

Fig. (4) A two-channel synthesis Filter bank to compute the IDWT

Together, Eq.s (11a), (11b) and (12) form the DWT and the IDWT. These discrete time algorithms with filter bank implementations are used in wavelet modulation.

The wavelet modulated signal to be transmitted, $s(t)$, can be generated by:

$$s(t) = a^{-H} y(at) \qquad (15)$$

where $x[n]$ is the data that is modulated onto the wavelet at different scales $\beta=2^{2H+1}$ where H refers to the degree of the homogeneous signal. A homogeneous signal $y(t)$ satisfies the self-invariance property:

$$y(t) = a^{-H} y(at) \tag{16}$$

where $a>0$ [1]. I take $H=-1/2$ so that $\beta=1$. Note that $s(t)$ is completely specified by $x[n]$. Contrarily, $x[n]$ is referred to as the generating sequence for the transmitted signal $s(t)$.

In a practical system, $x[n]$ is modulated onto a finite number of contiguous, octave-width frequency bands (i.e. m has finite limits and there are a finite number of scales available). Consequently, the transmitted signal $s(t)$ is given by [17]:

$$s(t) = \sum_{n=-\infty}^{\infty} \sum_{m \in M} \beta^{-m/2} x[n] 2^{m/2} \psi(2^m t - n) \tag{17}$$

where M is a finite set of contiguous integers.

For the data to be recovered at rate 2^m, the smallest baseband bandwidth that can be used is 2^{m+1}Hz. This results in a bandwidth efficiency of η_F=0.5bits/sec/Hz, which represents a disadvantage of wavelet modulation when compared to traditional modulation techniques like differential quadrature phase shift keying (QPSK) or 16-QAM with bandwidth efficiencies of η_F=2.0bits/sec/Hz and η_F=4.0bits/sec/Hz, respectively.

However, wavelet modulation has an advantage over traditional modulation techniques in its novel multirate diversity. For instance, in wavelet modulation, if some frequency bands are corrupted, then the message can still reach the receiver on one of the uncorrupted frequency bands (i.e. scales). Hence, wavelet modulation works well in fading environments where other modulation techniques suffer poor performance. In other words, only one copy of the message needs to get through.

These simulations have been carried out for two different sets of scales. Therefore, the scale parameter m takes on two sets of values as follows:

1. $m \in M$ where M={10, 11, 12, 13}; this corresponds to a data rate of R_b=1024bps for binary data at the coarse scale (m=10) and R_b=8192bps at the fine scale (m=13). For demodulation at the receiver, a baseband bandwidth of 2^{m+1}Hz is required [1]. Consequently, demodulation at scale m=13 requires a bandwidth of 2^{13+1}=16 kHz.

2. $m \in M$ where M={14, 15, 16, 17}; this corresponds to a data rate of R_b=16.384kbps for binary data at the coarse scale (m=14) and R_b=131kbps at the fine scale (m=17).

The data to be transmitted takes on one of two equally probable values:

$$x[n] \in \{+\sqrt{E_b}, -\sqrt{E_b}\} \tag{18}$$

where E_b is the energy per bit.

By comparing Eq.s (8b) and (15) and remembering that β=1, I note that the wavelet coefficients of $s(t)$ correspond to the data $x[n]$. Thus, $x[n]$ is used instead of s_l^m in Eq. (12) to obtain the approximation of $s(t)$ at scale m+1. Note that to compute the transmitted signal $s(t)$ I use the IFWT (Eq. 12) instead of Eq. (17), where a_n^{m+1} is the approximation of $s(t)$ at scale m+1.

The data to be transmitted ($x[n]$) is split into blocks of length L=1024. To begin the generation of $s(t)$, I begin at the coarse scale m=10; the data is convolved with the filter coefficients of the highpass filter, $g(n)$. Eq. (12) is simplified to:

$$a_n^{11} = \sum_l g(2l-n) x_l^{10} \tag{19}$$

where x_l^{10}, the data to be transmitted at scale 10, is given by the vector:

$x_l^{10} = x = [x[0], x[1], \ldots x[1023]]$

Twice the amount of data is required to modulate the data onto the next higher scale. A periodic replication of the data results in:

$x_l^{11} = [x\ x] = [x[0], x[1], \ldots x[1023], x[0], x[1], \ldots x[1023]]$

Then a_n^{12} (the approximation of $s(t)$ at scale 12) is obtained by Eq. 12 as:

$$a_n^{12} = \sum_l h(2l-n) a_l^{11} + g(2l-n) x_l^{11} \tag{20}$$

A view of the transmitted signal in the time-frequency plane is shown in Fig. (5). At scale 11 there is twice the amount of data at scale 10. Eq. (20) is repeated until the coefficients at scale 14, a_n^{14}, are obtained. These coefficients are iterated through the filter bank again with x_l^m=0 until approximation coefficients at scale 17 (a_n^{17}) are obtained. This results in a close approximation to the signal $s(t)$ with a sampling rate of 131072 samples/sec and this signal is then transmitted over the channel to the receiver.

Fig. (6) presents a block diagram for the implementation of the wavelet modulation simulator. The IDWT (implemented using the IFWT) performs the function of the transmitter and the DWT (implemented using the FWT) performs the function of the receiver. The decision device estimates the transmitted bit from the received data. If the received data is greater than zero, then the transmitted bit is $+\sqrt{E_b}$; if not, then the transmitted bit is $-\sqrt{E_b}$. The data comparator/verification step compares the received data with the transmitted data and determines the error rate. An error occurs if the received bit does not match the transmitted bit. In practice, the output signal $s(t)$ would be multiplied by a carrier at some pass-band frequency (ω_c) to obtain the band-pass signal.

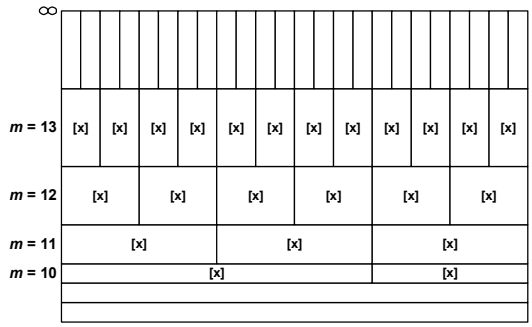

Fig. (5) Time-frequency portrait of the transmitted signal *s*(*t*). [*x*] represents data blocks of length *L*=1024 bits

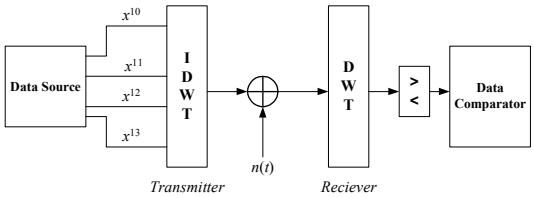

Fig. (6) Block diagram of WM simulator with an additive white Gaussian noise channel

The scaling constants α_0 and α_1 in Eq. (3) were 0.707 and 0.707, respectively, to give a main (carrier) ray to secondary (delayed) ray power ratio of 0dB, i.e.

$$E\{\alpha_0^2 R_0(t)^2\}E\{\alpha_1^2 R_1(t)^2\}=1 \quad (21a)$$

or

$$C/D = 0 \text{ dB} \quad (21b)$$

where C is the power in the main ray and D is the power in the delayed ray). The channel coefficients are normalized such that the average signal energy at the input to the channel is the same as the energy at the output. Recall that τ in Eq. (3) is $0.5T_{Si}$, where $12 \le i \le 17$ (T_{Si} refers to the bit period at scale i) and τ and σ_τ are related by $\sigma_\tau=\tau^2$. The r.m.s delay spread was varied from 1.9μs ($\tau=0.5T_{S17}$) to 61μs ($\tau=0.5T_{S12}$). Coherent demodulation was performed at the receiver for all transmitted scales.

For Gaussian distributed noise, the error probability can be calculated using the Q function defined by [18]:

$$Q(x)=\frac{1}{\sqrt{2\pi}}\int_x^\infty \exp\left(\frac{-t^2}{2}\right)dt \quad (22)$$

The function $Q(x)$ represents cumulative values of the Gaussian distribution.

The SNR of the channel at the receiver is usually the factor that determines the ease with which signal can e recovered. However, for a digital signal, it is the energy per bit and how much bandwidth is used, rather than the average signal and noise powers, that are the critical factors in determining how much of a problem the noise might cause. Hence, the ratio of signal-power-to-noise-power is better described by the ratio of signal energy per bit to thermal noise power per Hz (E_b/N_0) where $E_b=\boldsymbol{S/K}$ is the ratio of the signal power $\boldsymbol{S}$ to the data rate $\boldsymbol{K}$ (not the signal element rate), $N_0=\boldsymbol{N/B}$ is the noise power per Hz, where $\boldsymbol{N}$ is the total noise power and $\boldsymbol{B}$ is the bandwidth of the channel. Hence, E_b/N_0 is a measure of the worth of a channel used for digital signals, just as SNR is a measure of the worth of a channel used for analog signals.

For unipolar signaling, the bit error rate (BER) and E_b/N_0 are related by [18]:

$$BER = Q\left(\sqrt{a\frac{E_b}{N_0}}\right) \quad (23)$$

where a is a constant determined by the line coding scheme.

3. Results and Discussion

The inter-symbol interference (ISI) adversely impacts scales 16 and 17, but affects scale 14 to a comparatively lesser degree. Scales 14 and 15 show better performance than BPSK. This unique characteristic of wavelet modulation can be exploited to obtain better BER performance in mobile environments. For instance, if the worst case delay spread ($\sigma_{\tau max}$) of a particular environment were known, then the demodulation would be performed at the scales where the channel is flattest (i.e. scales where $T_{Si} \ge 10\sigma_{\tau max}$).

Now consider four different scales; scales 10 through 13 are transmitted over the frequency-selective channel. The r.m.s delay spread is 15.3μs which is $0.125T_{S13}$ ($\tau=0.25T_{S13}$). Fig. (7) depicts the BER performance. Scales 10 and 11 show error floors lower than 10^{-2}. Scales 12 and 13 display poorer BER performance since the ISI is larger at those scales.

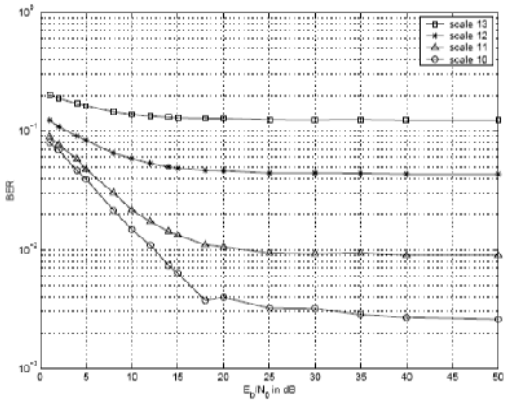

Fig. (7) Bit Error Rate (BER) vs. E_b/N_0 in a frequency selective, slow fading channel with f_d=60Hz and σ_τ=15.3μs=0.125T_{S13} (τ=30.5μs=0.25T_{S13})

Further simulations were performed for larger r.m.s delay spreads. Fig. (8) shows the BER performance for all scales when the r.m.s delay spread is $0.25T_{S12}$ ($\tau=0.5T_{S12}$). In Fig. (8), scales 11, 12 and 13 perform poorly while scale 10 shows a slightly better performance.

Furthermore, scale 13 has a lower error floor than scale 12.

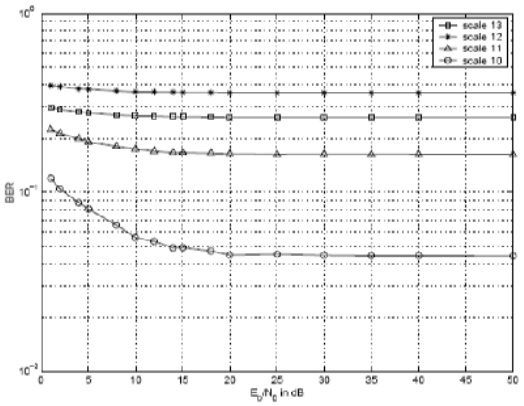

Fig. (8) Bit Error Rate (BER) vs. E_b/N_0 in a frequency selective, slow fading channel with f_d=60Hz and σ_τ=61μs =0.25T_{S12} (τ=0.5T_{S12})

When comparing both figures to each other, a gradual degradation of performance is seen for scale 10 demodulation as the delay τ is increased; scale 10 shows the best performance in Fig. (7) (i.e. for σ_τ=0.125T_{S13}) and the worst performance in Fig. (8) (i.e. for σ_τ=0.25T_{S12}). This is due to the increase in ISI for scale 10 data as the delay between the paths is gradually increased. At σ_τ=0.25T_{S12} (Fig. (8)), the second ray is delayed by half a symbol at scale 12 resulting in the distortion of the received signal at that scale and at scale 10 (due to ISI) from which the receiver cannot recover.

Furthermore, assuming a minimum BER of 10^{-2}, it is observed that the number of scales that can be used for demodulation decreases as the value of τ is increased. In particular, for τ=0.25T_{S13} (Fig. (7)), scales 10 and 11 can be used for demodulation. Hence, an intelligent selection of demodulation scales at the receiver can result in superior BER performance.

4. Conclusions

When the delay spread of a particular environment is known, the demodulation would be performed at the scales where the channel is flattest. It was observed that the number of scales that can be used for demodulation decreases as the value of the mean excess delay is increased. Since the results for the 120Hz channel do not vary appreciably from that which was observed for the 60Hz channel, it can be concluded that the limit on the BER is due to the ISI in a frequency-selective channel.

References

[1] G. Wornell and A. Oppenheim, *IEEE Trans. Information Theory*, 38 (1992) pp.785-800.

[2] H.S. Ptasinski and R.D. Fellman, "Implementation and simulation of a fractal modulation communication system", *Proc. IEEE SUPERCOMM/International Communications Conference*, 3 (1994) pp.1551-1555.

[3] D. Cochran and C. Wei, "A wavelet-based multiple-access spread spectrum modulation scheme", *13th Annual IEEE International Conference on Computers and Communications*, (1994), pp.461-464.

[4] E.J. Yi and E.J. Powers, "Wavelet-based orthogonal modulation code", *Proc. 33rd Asilomar Conference on Signals, Systems and Computers*, (1999) pp.674-692.

[5] R.H. Clarke, *Bell Systems Technical Journal*, 47 (1968) pp.957-1000.

[6] J.G. Proakis, S. Srinidhi and M. Stojanovic, "Wavelet based modulation for frequency hopped spread spectrum communications", *49th IEEE Vehicular Technology Conference*, 2 (1999) pp.904-908.

[7] H.M. Newlin, "Developments in the use of wavelets in communication systems", *Proceedings of MILCOM*, (1998) pp.343.349.

[8] G. Bi, W. Yang and T.P. Yum, "A multirate wireless transmission system using wavelet packet modulation", *47th IEEE Vehicular Technology Conference*, (1997) pp.368-372.

[9] G. Karabulut and A. Yongacoglu, "Additive model for Rayleigh fading channel", *Online article* (2005).

[10] M.J. Gans, *IEEE Trans. Vehicular Technol.*, VT-21 (1972) pp.27-38.

[11] C.C. Tan and N.C. Beaulieu, *IEEE Trans. Commun.*, 48(12) (2000), pp.2032-2040.

[12] T. Rappaport, "**Wireless Communications**", Prentice Hall (NJ), 1st edition, 1996.

[13] B. Sklar, *IEEE Communications Magazine*, 35(7) (1997) pp.90-100.

[14] S. Siedel, T. Rappaport and R. Singh, *IEEE Trans. Vehicular Technol.*, 39(2) (1990) pp.132-139.

[15] T. Rappaport, V. Fung and B. Thoma, *IEEE Trans. Inform. Theory*, 11(3) (1993) pp.393-405.

[16] I. Daubechies, **"Ten Lectures on Wavelets"**, SIAM (Philadelphia, PA), 1st edition, 1992.

[17] M.J. Usher and C.G. Guy, **"Information and Communication for Engineers"**, Macmillan Press, Ltd. (Hong Kong) (1997), pp.158-161.

[18] M. Wu, Y.H. Chew and T.T. Tjhung, *Int. J. Wireless Opt. Commun.*, 1 (2003) pp.41-52.

Hussain J. Hameed
Ahmed M. Jasim

Department of Mechanical Engineering, College of Engineering, University of Babil, Hilla, Babil, IRAQ

Densification Behavior and Dielectric Properties of Low-Temperature Corderite Ceramics

The cordierite ceramics were prepared from the waste of porous ceramics then the densification behavior and dielectric properties of cordierite ceramics adding three different proportions of $CaO–B_2O_3$ glass were investigated. Their crystalline phases, densification parameters, dielectric properties were introduced. The densities of all samples firstly increased and then decreased. The crystalline phase of samples was cordierite. The materials had a low dielectric constant and a low dielectric loss [ε~5, tan δ ~ (2-3) $x10^{-3}$, at about 10GHz]. The best properties were obtained for the sample with 15 wt% $CaO–B_2O_3$ glass added and sintered at 1020°C.

Keywords: Corderite ceramics, $CaO–B_2O_3$ glass, Dielectric properties, Sintering
Received: 20 April 2008, Revised: 20 May 2008, Accepted: 20 June 2008

1. Introduction

The demand for low-dielectric-constant, low-temperature cofired ceramics (LTCC) packaging is increasing with the development of high-frequency communication and electronic surface mount technology. However, high temperature is needed for sintering of most of the microwave dielectric ceramics [1-2]. Many low-melting temperature glasses are added to ceramics to reduce the sintering temperature in order to solve this problem [3-5].

As cordierite ceramic has a low dielectric constant (ε~5-6), high resistivity, good thermal and chemical stability, and a low thermal expansion coefficient, it is an alternative material to be used as a substrate substituting for alumina [6-8]. However, cordierite ceramics have a very narrow sintering temperature range and are not easily sintered below 1000°C without any sintering aids; its sintering temperature is about 1500°C. Some sintering aids can improve the sintering ability of cordierite ceramics, but also damage its properties, such as thermal expansion and dielectric constant [9-10].

In this work, the waste materials generated from the process of producing porous cordierite ceramics are chosen as the raw materials for reducing the cost. The purpose of this work is to introduce the densification and dielectric properties of cordierite ceramics with different glass contents under different sintering conditions.

2. Experimental Methods

CB glass with the composition of CaO 45mol%, B_2O_3 55mol%, using $CaCO_3$ and H_3BO_3 as the raw materials, was prepared by melting in a platinum crucible at 1100°C for 1 h, and the glass was quenched in water into fragments, which were then pulverized and screened to become the CB glass powders. The composition of the waste of porous cordierite ceramics is shown in Table (1). Three different ratios of glass and cordierite ceramics were mixed; the compositions of samples are listed in Table (2). The mixtures were ball milled for 3 h, then dried at 120°C and granulated with poly(vinyl alcohol) (PVA). The green powders were shaped by uniaxial pressing at 1000kg/cm^2. These samples were sintered at different temperatures, different binder burning temperatures (400, 450, 500, and 550°C, with a heating rate of 3°C/min) and different heating rates (1, 3, 5, and 8°C/min, with a binder burning temperature of 500°C).

Table (1) Composition of the cordierite ceramics waste (wt%)

	Composition			
	MgO	Al_2O_3	SiO_2	Fe_2O_3
Content	13.63	34.90	49.42	0.11

Table (2) Composition of the cordierite ceramics with different amounts of CB glass (wt%)

	Cordierite ceramics	CB glass
CB_{10}	90	10
CB_{15}	85	15
CB_{20}	80	20

Differential thermal analysis (DTA) was carried out in an alumina crucible using Al_2O_3 as the reference material in the NETZSCHSTA429C analyzer, with a heating rate of 10°C/min. Archimedes' method was used

to measure the apparent densities. The crystalline phases of samples were identified using a Rigaku RAX-10 diffractometer with a conventional Cu K-radiation system. The microwave dielectric properties of sintered samples were measured in the frequency range of 9-11 GHz using a network analyzer (Agilent HP8363A).

3. Results and Discussion

Fig. 1(a) shows the thermal properties of CB glass. The glass transition temperature (T_g), crystallization temperature (T_c), and melting temperature (T_m) of CB glass were 640, 795, and 970°C, respectively. As the T_g, T_c, and T_m of glass were low, it produced a liquid phase in the densification process to reduce the sintering temperature of samples, which was suitable for LTCC application. From the DTA curve of the cordierite ceramic with different amounts of glass, as shown in Fig. 1(b), no obvious peaks could be observed. This shows that the reaction of cordierite ceramic with CB glass did not occur during the sintering process, with the results observed by Jean and Gupta [11].

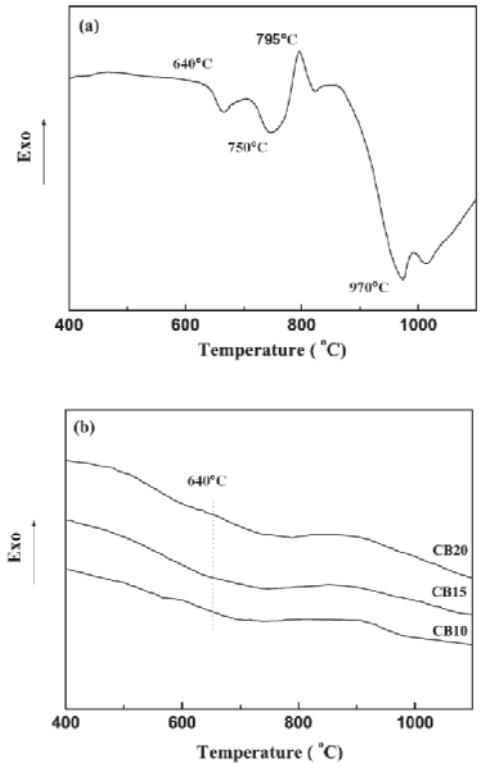

Fig. (1) DTA curves of (a) CB glass and (b) cordierite ceramic with different amounts of glass

Fig. (2) shows s of different compositions of samples sintered at different temperatures for 2h. With increasing sintering temperature, the densities of the samples having the same composition firstly increased and then decreased. CB glass and cordierite ceramics did not react in the sintering process. Therefore, the reason for the variety may be caused by the porosity variation of the samples.

The optimal sintering temperature of samples decreased gradually as the CB glass content increased. The maximal densities of CB10, CB15, and CB20 were 2.46, 2.42, and 2.33g/cm^3, at 1060, 1000, and 940°C, respectively. It was considered that CB glass produced a liquid phase in the densification process of the samples and greatly reduced the sintering temperature.

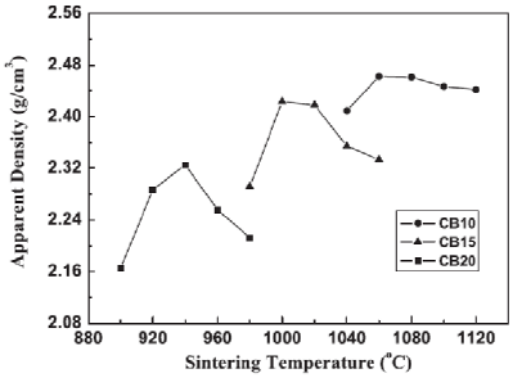

Fig. (2) Apparent densities of the samples as a function of sintering temperature for 2h

The same trend was exhibited in the patterns of dielectric loss; the dielectric loss of all samples firstly decreased and then increased. The minimal dielectric losses of CB10, CB15, and CB20 were $2.34\text{x}10^{-3}$, $2.79\text{x}10^{-3}$, and $3.17\text{x}10^{-3}$, obtained at 1060, 1020, and 940°C, respectively. Among all samples, CB15 had better properties, considering both sintering properties and dielectric properties. Thus, CB15 sintered at 1020°C was chosen to investigate the effect of heating rate and binder burning temperature on the properties of materials.

The density, linear shrinkage rate and dielectric properties of CB15 sintered at 1020°C with different heating rate are shown in Table (3). Table (4) shows the properties of the CB15 sample sintered at 1020°C with different binder burning temperatures. It can be obviously observed that the CB15 sample (the binder burning temperature is 500°C, with a heating rate of 3°C/min) had the optimal properties (ε~5.14, tan δ~$2.23\text{x}10^{-3}$ at 10.328GHz), as a low dielectric constant is required to obtain a higher selfresonance frequency for the materials used for the MLCIs [12].

Table (3) Properties of sample CB_{15} sintered at 1020°C with different heating rates

Heating Rate (°C/min)	Linear Shrinkage Rate (%)	Density (g/cm^3)	Dielectric Constant	Dielectric Loss ($x10^{-3}$)	Measuring Frequency (GHz)
1	17.55	2.44	5.15	2.67	10.446
3	17.35	2.43	5.14	2.23	10.328
5	17.85	2.42	5.13	2.79	9.801
8	17.45	2.43	5.15	2.95	9.933

Table (4) Properties of sample CB_{15} sintered at 1020°C with different binder burning rates

Binder Burning Temperature (°C)	Linear Shrinkage Rate (%)	Density (g/cm^3)	Dielectric constant	Dielectric Loss ($x10^{-3}$)	Measuring Frequency (GHz)
400	17.55	2.42	5.10	2.92	9.542
450	17.60	2.42	5.11	2.82	9.796
500	17.35	2.43	5.14	2.23	10.328
550	17.65	2.42	5.11	2.55	9.724

4. Conclusions

From the results obtained in this work, we conclude that $CaO–B_2O_3$ glass did not react with cordierite ceramic in the sintering process. The glass produced a liquid phase in the densification process and greatly reduced the sintering temperature of samples. A higher amount of $CaO–B_2O_3$ glass added increased the dielectric loss of samples. With increasing sintering temperature, the densities and dielectric constants of all samples firstly increased and then decreased. The dielectric losses of CB10, CB15, and CB20 reached their lowest values at sintering temperatures of 1060, 1020, and 940°C, respectively. The CB15 sample sintered at 1020°C for 2h (at a binder burning temperature of 500°C, and a heating rate of 3°C/min) had better properties.

References

1. P.H. Sun et al., *Jpn. J. Appl. Phys.*, 37 (1998) 5625.
2. C.L. Huang, R.Y. Yang and M.H. Weng, *Jpn. J. Appl. Phys.*, 39 (2000) 6008.
3. R.R. Tummala, *J. Am. Ceram. Soc.*, 74 (1991) 895.
4. J.H. Jeana and T.K. Gupta, *IEEE Trans. Component Packag. Manuf. Technol.*, 17 (1994) 228.
5. Y.J. Seo and J.H. Jung, *J. Am. Ceram. Soc.*, 90 (2007) 649.
6. S.H. Knickerbocker, A.H. Kumar and L.W. Herron, *Am. Ceram. Soc. Bull.*, 72 (1993) 90.
7. G.H. Chen and X.Y. Liu, *J. Alloys Compd.*, 431 (2007) 282.
8. M.A. Subramanian and U. Chowdhry, *Bull. Mater. Sci.*, 16 (1993) 665.
9. M. Awano, H. Takagi and Y. Kuwhara, *J. Am. Ceram. Soc.*, 75 (1992) 2535.
10. R.G. Chandran, K.C. Patil and G.T. Chandrappa, *J. Mater. Sci. Lett.*, 14 (1995) 548.
11. J.H. Jean and T.K. Gupta, *J. Mater. Sci.*, 27 (1992) 4967.
12. Z.X. Yue and J. Zhou, *J. Mater. Sci. Lett.*, 19 (2000) 213.

  PRINTED IN IRAQ

Optoelectronic Characteristics of As-doped Silicon Photodetectors Produced by LID Technique

Aseel A.K. Hadi [1]
Oday A. Hamadi [2]

[1] *School of Applied Sciences, University of Technology, Baghdad, IRAQ*
[2] *P. O. Box 55159, Baghdad 12001, IRAQ*

In this work, optoelectronics characteristics of arsenic-doped silicon photodetectors produced by laser-induced diffusion technique were introduced. Results explained that the parameters of the photodetectors depend on laser energy and substrate temperature. Maximum Responsivity was obtained for the photodetectors prepared by laser fluence of 9.08J/cm^2 at substrate temperature of 598K. The pulse response waveform of photodetectors illustrated that the rise time is not dominated by RC. Non-linearity deviation coefficient was improved by factors 2.1 for As-doped Si photodetectors when substrate temperature is raised from 300K to 598K.

Keywords: Silicon photodetectors, Photo-response, Laser-induced diffusion
Received: 15 April 2008, Revised: 25 May 2008, Accepted: 15 July 2008

1. Introduction

Many researchers have worked on the processing of semiconductors by pulsed laser-induced diffusion (LID) [1-4]. The major advantages of semiconductor junction devices such as photodetector, solar cells and optoelectronics using laser-induced diffusion and annealing are: (i) short processing time, (ii) ultra-shallow junction can be obtained, (iii) do not need post-diffusion heat treatment, (iv) offer excellent abruptness and junction depth control, (v) due to the localization of laser spot size on the semiconductor device, the minority-carrier lifetime of the substrate is reserved, (vi) high control of the sensitive area on the photodiode by controlling the laser spot size, (vii) capability to achieve high concentration doping (10^{17}-10^{19}cm^{-3}), (viii) dopants activate above the solid solubility limit [5-6].

Nd:YAG laser was widely used in silicon processing as the photon energy of this laser (1.17eV) is ideally matched to the energy bandgap of silicon (1.12eV at 300K) [7-8]. Previous works showed that the peak photoresponse of silicon photodiode fabricated by laser-induced diffusion was around 900nm [9]. Few studies have been reported on photoresponse of Si photodiodes fabricated by pulsed Nd:YAG laser-induced diffusion. These studies do not cover the comprehensive characterization of photodiode parameters at peak wavelength (900nm) [10-11].

In this paper, we report the results on arsenic-doped silicon photodiode at peak response prepared by long Nd:YAG laser pulses.

2. Experiment

The silicon substrates used in this work were (111)-oriented monocrystalline of n-type conductivity. The dimensions of the substarte were 1x1x0.05cm^3. The hole and electron concentration around $8.3\text{x}10^{14}$cm^{-3} and $1.4\text{x}10^{15}$cm^{-3}, respectively. The surface preparation consisted of mechanical polishing until mirror-like surface was obtained, then dipped in dilute HF acid to remove native oxide, and immediately loaded into thermal evaporation system which is then evacuated to pressure down to 10^{-6}mbar. High purity 50nm arsenic (99.99%) films were deposited on silicon substrates. Following deposition process, each sample was transferred to the pulsed laser system. The samples were irradiated under vacuum (10^{-2}mbar) using 300us pulse length from a 1064nm Nd:YAG laser. The pulse shape was approximately Gaussian in time (TEM_{00}). The pulse energy used in these experiments was ranging from 160mJ to 405mJ. The substrates were heated prior laser radiation with different temperatures (373–598)K using a halogen

lamp. The temperature was monitored by K-type thermocouple. The laser spot size was adjusted using a lens of 20cm focal length to be about $38.5x10^{-4}cm^2$. In order to increase the irradiated area (photodetector area) to $1cm^2$, overlapping laser pulses with 35% overlapping ratio.

Before making ohmic contacts, the samples were rinsed in NaOH to remove residual atoms of arsenic. Subsequently; ohmic contacts were made on n-type sides using Au electrodes. 200ns pulses of 904nm GaAlAs laser were employed to investigate the responsivity and the response speed of photodiodes (R_L=50Ω, V_R=5-30V) fabricated at various conditions. The pulse shape was recorded by 250MHz Tektronix storage oscilloscope.

3. Results and Discussion

Fig. (1) shows the electrical sheet conductivity of the processed region of silicon substarte as a function of laser fluence for As-doped n-Si samples. The main electrical characteristics of these diodes were presented in previous studies [12-14]. It is obvious that the sheet conductivity increases with laser fluence up to $9.17J/cm^2$ for As-doped Si. This is being to be the irradiation at optimum conditions, i.e, irradiation at laser melting threshold (LMT). At these conditions, the electrical activation of the dopants was very high. Further increasing of laser fluence resulted in increasing of the defects density in the processed region such as the vacancies induced in lattice during solidification process [15]. These defects in turn lead to decrease sheet conductivity of the layer.

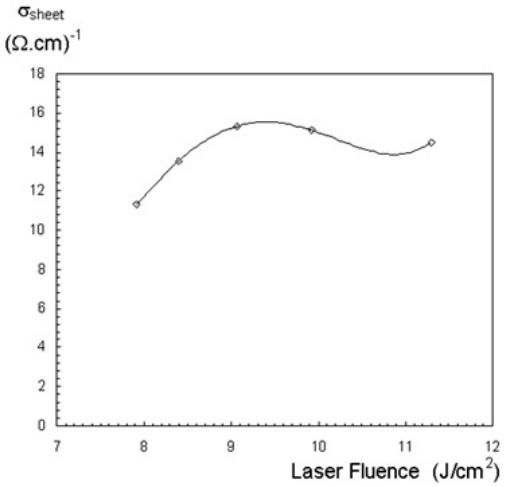

Fig. (1) Variation of sheet conductivity with laser fluence

Fig. (2) demonstrates the responsivity in the reverse biasing for p-n As-doped Si photodetectors fabricated with different laser fluences at 300K. Irradiation with low laser fluence results in poor junction and hence no responsivity was observed.

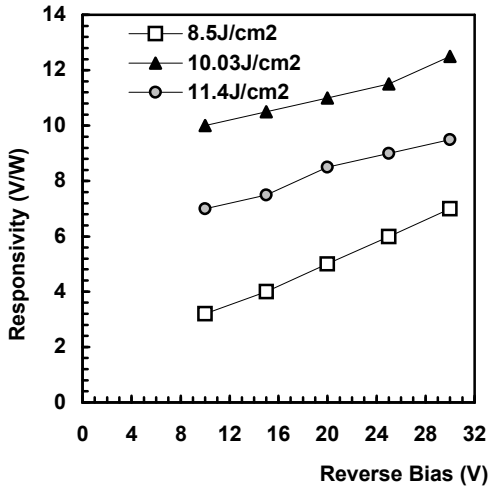

Fig. (2) The spectral responsivity as a function of reverse bias voltage at 300K for As-doped Si photodetector

The peak responsivity obtained at $10.03J/cm^2$ laser fluence for As-doped n-Si photodetectors, where these laser fluences represent the melting threshold (irradiation condition with minimum defects) [7]. The responsivity is competitive to that of silicon p-n junction photodiodes made by other methods. Working at laser fluence higher than LMT leads to decrease the responsivity and this may be properly due to four reasons: (i) decreasing of the junction depth due to decreasing of the sheet conductivity [16], (ii) structural defects such as cracks, ripple, recombination and trapping centers, (iii) vaporization of dopant materials, and (iv) highly non-equilibrium process occurring during fast solidification process [17].

The effect of substrate temperature on the responsivity versus bias voltage is presented in Fig. (3). Increasing substrate temperature to 598K causes an increase in responsivity by a factor of 5 for As-doped Si detectors. This is mainly due to the decreasing of solidification rate of the processed region at high T_s [18-19]. On the other hand, the laser melting threshold will be low at high T_s because of increasing absorption coefficient α which in turns decreasing the laser fluence needed for melting and hence producing doped region with minimum structural defects [20].

The rise time versus bias voltage plots for photodetectors prepared at different conditions at room temperature are presented in Fig. (4). No significant variation in the rise time as the reverse bias voltage varies was observed. This behavior is similar to that of diffused-silicon photodiodes and it is evident that the doping

laser fluence plays major role to affect the rise time of photodiodes. The best rise time of 600ns at 30V was obtained for As-doped Si photodiode fabricated at 10.03J/cm^2. It is clear that the rise time is increased with the increasing laser fluence. This is can be attributed to the high density of defects created in depletion region which can in turn leads to large leakage current [14]. The rise time is directly related to the concentration of active As impurities, which strongly depend on the laser fluence. Furthermore, the rise time of photodiode is significantly decreased with reverse bias voltage.

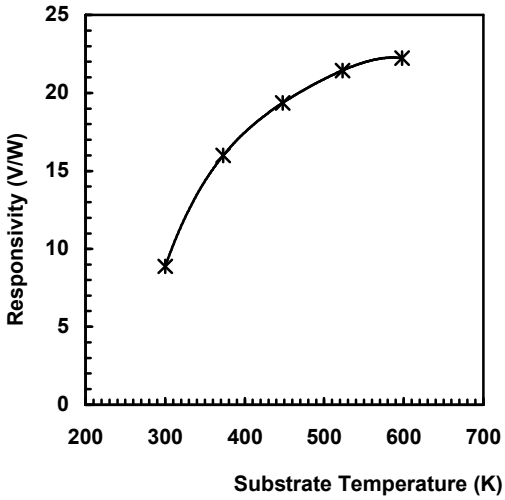

Fig. (3) Voltage responsivity versus substrate temperature for photodetector fabricated at LMT

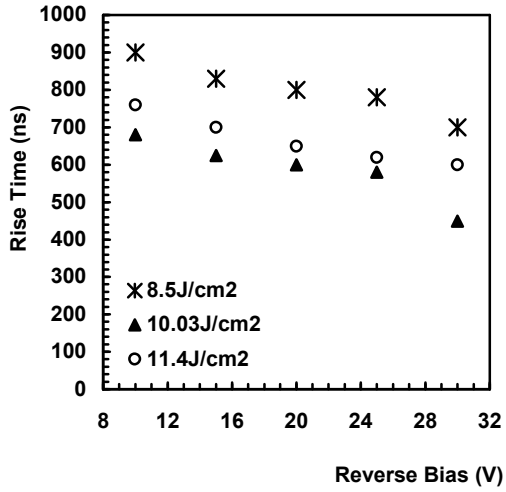

Fig. (4) Effect of biasing voltage on the rise time characteristics for As-doped Si photodiodes

The effect of substrate temperature on the rise time of p-n photodiodes is obvious in Fig. (5). Rising T_s resulted in decreasing of the rise time of the photodiodes. These results are competitive and encouraging with respect to phosphorus-diffused silicon junction and they can be attributed to the role of substrate heating in reducing the structural defect as well as because the carriers diffusion length will be high when rising T_s.

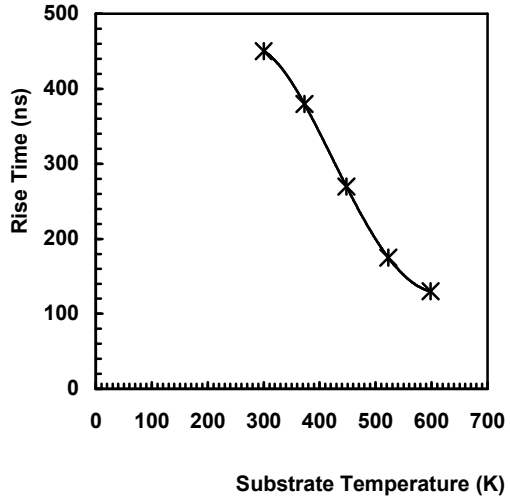

Fig. (5) The dependency of rise time on substrate temperature

Significant improvement was observed in the linearity of photodiode at T_s=598K. All previous mentioned measurements are repeated after six months. No significant degradation in the characteristics of the fabricated photodiodes was observed. The structural defects, such as cracks, recombination and trapping centers, clusters, segregation effects and point defects, are at their minimum levels for photodiodes prepared at substrate temperature of about 350°C.

4. Conclusion

High-response 1cm^2 area silicon photodiodes at 904nm can be made with aid of laser-induced diffusion (LID) technique. Such photodiodes has an advantage in their production without using antireflection coating, which reduces their production cost and architecture. The substrate heating plays an essential role in improving the photo-response and response speed of photodetectors. The structural defects accompanying pulsed-laser treatment affect both the pulse shape waveform and the response speed. The effect of rapid thermal annealing on the photodetector characteristics after laser-induced diffusion is underway.

References

1. Y. Miyata, M. Furuta and T. Kawamura, *J. AppI. Phys.*, 73, 327 (1993).

2. P. M. Smith, P. G. Carey, and T. W. Sigmon, *Appl. Phys. Lett.*, 70, 342 (1997).
3. Y. Takamura, S. Jang, P. B. Griffin and J. D. Plummer, *Mater. Symp. Proc.*, 669 (2001).
4. S. Baek, T. Jang, H. Hawang, *Appl. Phys. Lett.*, 80, 2272 (2002).
5. H. Tsukamoto, H. Yamamoto, T. Noguchi, *Jpn. J. Appl. Phys.*, 35, 3810 (1996).
6. V. Privitera, C. Spinella, G. Fortunato, L. Mariucci, *Appl. Phys. Lett.*, 77, 552 (2000).
7. R. A. Ismail and W. K. Hamoudi, *J. Eng. Technol. (Published in Iraq)*, 19, 119 (2000).
8. W. K. Hamoudi, and R. O. Dala, *J. Mater. Sci.*, 45, 1 (2000).
9. A.A.K. Hadi, M.Sc Thesis, University of Technology, Baghdad, Iraq, 1999, p. 110.
10. Y. Matsuoka, and A. Usama, *J. Phys. D: Appl. Phys.*, 7, 1259 (1974).
11. E. Fograssy, R. Stucky, and M. Toulemonde, *J. Appl. Phys.*, 54, 5059 (1983).
12. R.A. Ismail and A.A. Hadi, *Turkish J. of Phys.*, 27, 1 (2003).
13. R.A. Ismail et al., *Euro. J. Phys. Appl. Phys. (EPJAP)*, 38 (2007) 197-201.
14. R.A. Ismail, *Int. J. Modern Phys. (IJMPB)*, 19(31) (2005) 4619-4628.
15. G. Minnino, V. Privitera, A. Magna, *Appl. Phys. Lett.*, 86, S1909 (2004).
16. S. Earles, M. Laww, R. Brindows, K. Jones, S. Talwar, S. Corcoran, *IEEE Trans. Electron. Devices*, 49, 1118 (2002).
17. V. M. Artyunyan, A. P. Akhoyan, Z. N. Adamyan, R. S. Barsegyam, *Technical Physics*, 46, 198 (2001).
18. J. Narayan, *J. Cryst. Growth*, 59, 583 (1982).
19. H. Kuriyama, *Jpn. J. Appl. Phys.*, 30 (12B), 3700 (1991).
20. R. A. Ismail, *J. Eng. Technol. (Published in Iraq)*, 19, 148 (2000).

  PRINTED IN IRAQ

Mothana I. Ali
Saad M. Jasim
Qasim A. Sabbar

Department of Physics, College of Science, Alqadisiyah University, Dewanyah, IRAQ

Electrical Properties of Cu_2O Films Prepared by Electro-Deposition Method

In this work, the electrical properties of electrodeposited Cu_2O in aqueous solutions were investigated. The results explained good stability under illumination conditions at negative potentials. The diffusion length of electrons in the sample was determined to be about 10-100nm. The deposited Cu_2O films could be a promising material in electrochemical photovoltaic cells technology.

Keywords: Cu_xO, Semiconductor structures, Photoelectric properties, Diffusion length
Received: 10 April 2008, Revised: 20 June 2008, Accepted: 20 July 2008

1. Introduction

Cuprous oxide as a material for the conversion of solar energy into electrical or chemical energy has received relatively little attention. Several papers have considered the use of the material in a solid-state photovoltaic cell, such as Schottky barrier device obtained by applying metal contacts to the Cu_2O. The oxide is very easily reduced and in all cases, a copper rich phase formed near the Cu_2O/metal interface [1-3].

Another option would be to use the material in a photoelectrochemical (PEC) cell. A problem might be the limited stability of Cu_2O in aqueous solutions. Cu_2O is stable only in a limited pH range [4]. The redox potentials for the reduction and oxidation of the monovalent copper oxide lie well within the band-gap, making possible the decomposition reactions by photogenerated electrons or holes thermodynamically [5]. Furthermore, single crystalline Cu_2O is being reduced to copper under photocathodic conditions [6]. However, a paper was published [7] indicating that illuminated Cu_2O particles could show good stability while acting as a catalyst for water splitting. Hydrogen and oxygen were evolved in a rapidly stirred, illuminated suspension of millimeter-sized particles, without a noticeable decrease in activity for a period over 1900 hours.

A second paper was published later in which the water splitting was found to continue for many hours after the light was turned off. The authors tried to explain their results by proposing that the mechanical energy supplied by the stirring was converted into chemical energy, with the oxide acting as a catalyst [8].

In this paper, we study the electrical and chemical properties of Cu_2O deposited in aqueous solutions. The photocathodic reduction reactions of oxygen and the 1,1-dimethyl-4,4-bipyridinium cation (methylviologen, MV21) will be described. We will consider the decomposition reactions of Cu_2O in aqueous environment and its potential for direct photochemical water splitting or use in a PEC solar cell.

2. Experiment

Cu_2O was deposited on transparent, fluorine-doped SnO substrates by reduction of Cu^{2+} from a saturated Cu(II) lactate solution. Layers with a thickness up to ~10um could be grown with a deposition efficiency of about 0.9. This deposition efficiency was determined by measuring the charge for deposition and subsequent anodic dissolution. The layer thickness was determined from the interference patterns in the absorption spectra. The Cu_2O used in the present work was grown at pH 11 and 558°C, with a current density of 0.2mA/cm^2. A band-gap of 2.0eV was estimated from the optical absorption, in good agreement with literature values. Due to CuO, we did not observe absorption at wavelengths longer than 600nm. The electrical and chemical properties of the Cu_2O layers did not change for months despite they were kept in air.

The measurements were performed in a three electrode setup, using a potentiostat, a large area platinum counter electrode and a saturated calomel reference electrode (SCE). The aqueous electrolyte solutions contained 0.5M Na_2SO_4 or 40mM $MVCl_2$ in 0.5M Na_2SO_4, and were bubbled with either air or argon.

3. Results and Discussion

Fig. (1) shows the I-V characteristics of a 0.5μm thick Cu_2O electrode in 0.5M Na_2SO_4 solution in the dark. At potentials above 0.0V an anodic current was observed, corresponding to the oxidation of the Cu_2O (all redox potentials

mentioned in this paper are *vs*. SCE, refer to pH 7 and were taken from [10]):

$$Cu_2O + 2OH^- + 2h^+ \rightarrow 2CuO + H_2O \qquad E = -0.05V \quad (1)$$

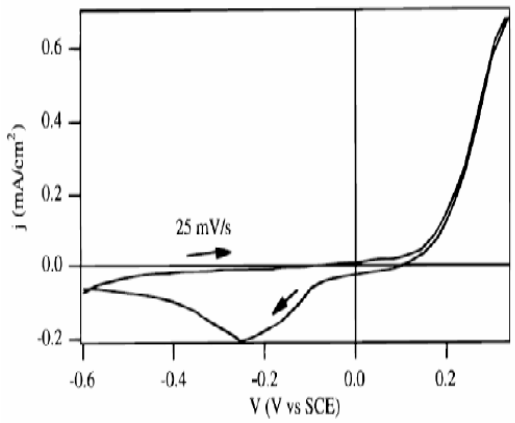

Fig. (1) I-V characteristics of a 500nm thick Cu_2O layer in 0.5M Na_2SO_4 aqueous solution

In a Na_2SO_4 aqueous solution the CuO slowly dissolves. The CuO can be partly reduced by scanning back to negative potentials. In the presence of oxygen, a small steady-state cathodic current was observed. When the argon was sluiced through solution, this dark current could be reduced to less than 1μA/cm^2. At potentials more negative than -0.6V *vs*. SCE a fast increasing cathodic current was found due to the reduction of the oxide to copper.

Under illumination, a large cathodic photocurrent was observed with an air-saturated solution under strong convection. When the argon was carefully sluiced through solution, the cathodic photocurrent was very low (~1μA/cm^2). It is clear that the photocurrent observed in air-saturated solution is due to oxygen reduction:

$$O_2 + 2H_2O + 2e^- \rightarrow H_2O_2 + 2OH^- \qquad E = +0.03V \quad (2)$$

The hydrogen peroxide is very likely reduced further to water [11]. The reduction of oxygen to hydrogen peroxide has been studied for instance at illuminated p-GaAs, GaP and n-type and p-type InP [12-14]. It is a multistep reaction involving a HO_2**.** intermediate. Current doubling was observed at low light intensities, as the HO_2**.** intermediate could inject a hole into valence band.

Fig. (2) shows the I-V characteristics for a 0.5μm thick Cu_2O electrode under chopped illumination at 350nm. The photocurrent (I_{ph}) starts at a potential between 0.0 and 0.1V and increases continuously with decreasing potential. Obviously, the photocathodic reduction of oxygen on Cu_2O is extremely efficient. The photocurrent was constant over long periods, even when photon flux exceeded the oxygen flux to electrode surface.

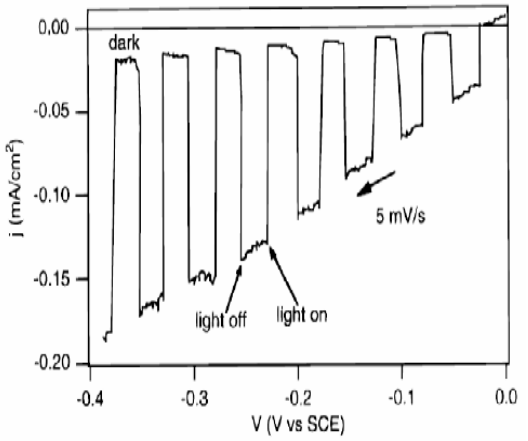

Fig. (2) I-V characteristics for a 500nm thick Cu_2O layer under chopped 350nm illumination in 0.5M Na_2SO_4 solution bubbled with air

Fig. (3) shows the I-V characteristics for a 0.5μm thick Cu_2O electrode in a 0.5M Na_2SO_4 aqueous solution bubbled with air in the presence of MV^{2+}. The photocurrent quantum efficiency at -0.4V *vs*. SCE was 0.2. The photocurrent decreased continuously with time. The current decayed to 50% of its initial value after the passage of about 12mC/cm^2. The photocathodic current has partly recovered after a period in the dark.

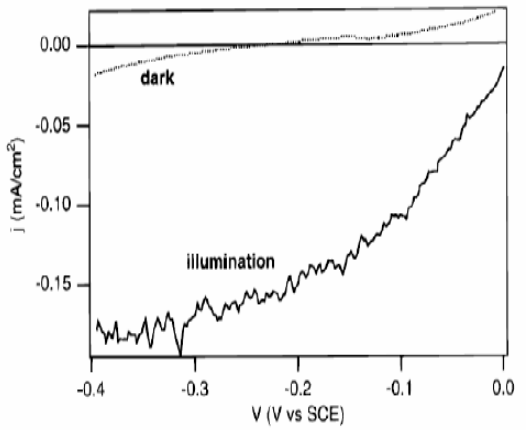

Fig. (3) I-V characteristics for a 500nm thick Cu_2O layer in the dark and under 350nm illumination. Electrolyte is 10mM MV^{2+} in 0.5M Na_2SO_4 solution bubbled with air

4. Conclusions

The properties of deposited Cu_2O were investigated. In the dark the oxide dissolves at potentials above 0.0V. A small cathodic dark current can be found due to the reduction of oxygen. In contrast to single crystalline Cu_2O, these deposited layers were stable under illumination. High efficiencies were found for the photocathodic reduction of oxygen and the

methylviologen cation. The diffusion length of minority charge carriers (electrons in the conduction band) is in the range of 10-100nm. No evidence was found for the reduction of water. Based on our results, it seems unlikely that water can be split photochemically at Cu_2O.

References

[1] R.N. Briskman, *Solar Energy Mater. Solar Cells*, 27 (1992) 361.

[2] L.C. Olsen, F.W. Addis and W. Miller, *Solar Cells*, 7 (1982-1983) 247.

[3] M. Fujinaka and A.A. Berezin, *J. Appl. Phys.*, 54 (1983) 3582.

[4] M. Pourbaix, *Atlas of Electrochemical Equilibria in Aqueous Solutions* NACE, Houston, TX (1974).

[5] H. Gerischer, *J. Electroanal. Chem.*, 82 (1977) 133.

[6] H.R. Schppel and H. Gerischer, *J. Bunsen-Ges. Phys. Chem.*, 75 (1971) 1237.

[7] M. Hara et al., *Chem. Commun.*, 357 (1998).

[8] S. Ikeda et al., *Chem. Commun.*, 2158 (1998).

[9] *Standard Potentials in Aqueous Solution*, A.J. Bard, R. Parsons and J. Jordan, Editors, IUPAC, New York (1985).

[10] J. Li and L. M. Peter, *J. Electroanal. Chem.*, 182 (1985) 399.

[11] 18. J. Li, R. Peat and L.M. Peter, *J. Electroanal. Chem.*, 200 (1986) 333.

[12] J.W.M. Jacobs and J.M.G. Rikken, *J. Electroanal. Chem.*, 258 (1988) 147 .

[13] A. Etcheberry, J. Gautron and J.L. Sculfort, *J. Electroanal. Chem.*, 247 (1988) 265.

[14] G. Schoenmakers, R. Waagenaar and J. Kelly, *J. Phys. Chem.*, 100 (1996) 1169.

Iraqi Journal of Applied Physics Letters

" INSTRUCTIONS TO AUTHORS "

CONTRIBUTIONS

Contributions to be published in this journal should be original research works, i.e., those not already published or submitted for publication elsewhere, individual papers or letters to editor.

SUBMISSION OF MANUSCRIPTS

Manuscripts should be submitted to one of the following addresses:

Dr. Raad Azzawi KHAMIS
Editor-in-Chief
Branch of Laser & Optoelectronics,
School of Applied Sciences,
University of Technology,
P. O. Box 35010,
Baghdad, IRAQ

Oday Ata HAMADI
Managing Editor
P. O. Box 55259,
Baghdad 12001, IRAQ
Tel.: +964-7901274190
Tel.: +964-7702523071
Email: ijaplett.editor@hotmail.com

MANUSCRIPTS

Two hard copies with soft copy on a compact disc (CD) should be submitted to Editor in the following configuration:

- Double-spaced one-side A4 size with 2.5cm (1") margins of all sides
- 12pt Times New Roman font (regular for text and bold for headings)
- Letters should not exceed 12 pages
- Manuscripts presented in English only are accepted
- Authors explain affiliations, addresses and emails. Email is necessary for correspondences. The corresponding author will be assigned by asterisk (star sign) to refer to its corresponding address
- English abstract not exceed 150 words
- 4 keywords (at least) should be maintained on (PACS preferred)
- Author(s) should express all quantities in SI units
- Equations should be written in equation form (*italic* and symbolic)
- Figures and Tables should be separated from text
- Figures and diagrams can be submitted in colors for assessment and they will be returned to authors after provide printable copies. Printing in colors imposes additional fees
- Charts should be indicated by the software used for
- Only original or high-resolution scanner photos are accepted
- References are written in titles, full-name authors, names of publications, years, volumes, issues and pages (from-to)
- Editorial Board has the rights to directly reject any article not prepared according to these instructions

PROOFS

Authors will receive proofs of papers and are requested to return one corrected hard copy with a WORD copy on a compact disc (CD). New materials inserted in the original text without Editor permission may cause rejection of paper.

COPYRIGHT FORM

Author(s) will be asked to transfer copyrights of the article to the Journal soon after acceptance of it. This will ensure the widest possible dissemination of information.

OFFPRINTS

Authors will receive offprints free of charge and any additional offprints can be ordered.

SUBSCRIPTION AND ORDERS

Annual fees (4 issues per year) of subscription are:

- 50 000 Iraqi dinars for individuals and students inside Iraq.
- 100 000 Iraqi dinars for institutions and establishments inside Iraq.
- 50 US$ for individuals and students abroad.
- 100 US$ for institutions and establishments abroad.

Orders of issues can be submitted by contacting the editor-in-chief or editorial secretary to maintain the address of issue delivery and payment way.

  PRINTED IN IRAQ

THE IRAQI JOURNAL OF APPLIED PHYSICS LETTERS
EDITORIAL BOARD

IJAPLett

COPYRIGHT RELEASE

Iraqi Journal of Applied Physics Letters (IJAPLett)

We, the undersigned, the author/authors of the article titled

……

……

……

……

that is presented to the Iraqi Journal of Applied Physics Letters (IJAPLett) for publication, declare that we have neither taken part or full text from any published work by others, nor presented or published it elsewhere in any other journal. We also declare transferring copyrights and conduct of this article to the Iraqi Journal of Applied Physics Letters (IJAPLett) after accepting it for publication.

The authors will keep the following rights:

1. Possession of the article such as patent rights.
2. Free of charge use of the article or part of it in any future work by the authors such as books and lecture notes without referring to the IJAPLett.
3. Republishing the article for any personal purposes of the authors after taking journal permission.

To be signed by all authors:

Signature:……..date: ……..

Printed name: ……..

Signature:……..date: ……..

Printed name: ……..

Signature:……..date: ……..

Printed name: ……..

Correspondence address:…….

…….

…….

Telephone:……Fax:…….email: ……

Note: Please, complete and sign this form and mail it to the below address with your manuscript

The Iraqi Journal of Applied Physics Letters,

P. O. Box 55259, Baghdad 12001, IRAQ
Email: ijaplett.editor@hotmail.com
Mobile: +964-7901274190

CONTENTS

VOL. 1 , NO. 2 , JULY-SEPTEMBER 2008

  PRINTED IN IRAQ